



RaBiT: Residual-Aware Binarization Training for Accurate and Efficient LLMs

Youngcheon You^{*1} Banseok Lee^{*1} Minseop Choi¹ Seonyoung Kim¹
 Hyochan Chong¹ Changdong Kim¹ Youngmin Kim^{†1} Dongkyu Kim^{†1}

Abstract

Efficient deployment of large language models (LLMs) requires extreme quantization, forcing a critical trade-off between low-bit efficiency and performance. Residual binarization enables hardware-friendly, matmul-free inference by stacking binary (± 1) layers, but is plagued by pathological feature co-adaptation. We identify a key failure mode, which we term **inter-path adaptation**: during quantization-aware training (QAT), parallel residual binary paths learn redundant features, degrading the error-compensation structure and limiting the expressive capacity of the model. While prior work relies on heuristic workarounds (*e.g.*, path freezing) that constrain the solution space, we propose **RaBiT**, a novel quantization framework that resolves co-adaptation by algorithmically enforcing a residual hierarchy. Its core mechanism sequentially derives each binary path from a single shared full-precision weight, which ensures that every path corrects the error of the preceding one. This process is stabilized by a robust initialization that prioritizes functional preservation over mere weight approximation. RaBiT redefines the 2-bit accuracy-efficiency frontier: it achieves state-of-the-art performance, rivals even hardware-intensive Vector Quantization (VQ) methods, and delivers a **4.49 \times inference speed-up** over full-precision models on an RTX 4090.

1. Introduction

Model compression is essential for efficient deployment of large language models (LLMs). While 4-bit quantization methods (Frantar et al., 2022; Lin et al., 2024) have emerged as a successful industry standard (Kwon et al., 2023; Zheng

et al., 2024), the relentless pursuit of greater efficiency is pushing the research frontier towards the 2-bit regime. This transition to lower bit compression introduces architectural trade-offs that characterize the current domain.

At the 2-bit frontier, two primary strategies present a choice between representational fidelity and hardware efficiency. Vector Quantization (VQ) methods typically yield high accuracy but incur hardware overhead due to lookup tables or complex rotations (Tseng et al., 2024a;b; Egiazarian et al., 2024). Conversely, residual binarization—stacking multiple binary layers—facilitates exceptional, matmul-free efficiency. However, this approach has struggled to preserve performance, due to fundamental training instabilities that prevent full potential realization (Bulat et al., 2024; Wang et al., 2024a; Tran & Nguyen, 2025).

The core promise of a residual architecture—that subsequent paths compensate for the errors of preceding ones—is fundamentally undermined by feature co-adaptation (Hinton et al., 2012), a pathological training dynamic where parallel components learn redundant features. In residual binarization, we identify a critical manifestation of this phenomenon, which we term **inter-path adaptation**. During standard quantization-aware training (QAT) (Bengio et al., 2013; Hubara et al., 2018), a structurally agnostic global gradient is simultaneously applied to all paths. This forces each path to learn redundant features in a race to minimize the global objective, overriding their intended compensatory roles. The result is a breakdown of the residual hierarchy that severely limits the model’s expressive power.

Previous efforts have employed heuristic constraints, such as path freezing (Bulat et al., 2024; Tran & Nguyen, 2025), which inherently limit the model’s capacity to derive an optimal joint solution. To address this, we propose **Residual-Aware Binarization Training (RaBiT)**, a QAT framework that resolves inter-path adaptation by design, as depicted in Figure 1. Instead of using independent latent weights, RaBiT maintains a single shared full-precision weight from which binary paths are sequentially derived on-the-fly, guided by learnable scales. This algorithmically enforces a residual hierarchy, training each path to correct

^{*}Equal contribution [†]Samsung Research, Seoul, Korea.

[†]Correspondence to: Dongkyu Kim <dongkyu.k@samsung.com>, Youngmin Kim <ym1012.kim@samsung.com>.

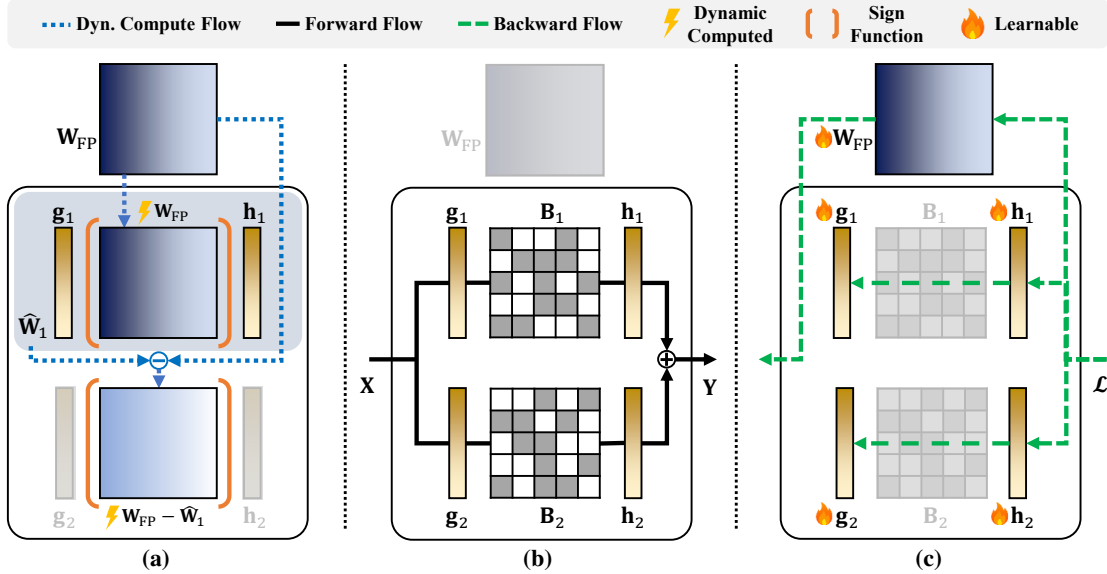


Figure 1. Overview of the RaBiT training framework. (a) **Dynamic Compute Process**: During training, binary paths are dynamically derived from a shared weight W_{FP} to enforce a residual hierarchy. (b) **Forward Pass**: For inference, these paths execute in parallel for matmul-free efficiency. (c) **Backward Pass**: Gradients from the loss \mathcal{L} update both the learnable scales (g_i, h_i) and the shared W_{FP} .

its predecessor’s error. Combined with a robust, function-aware initialization, RaBiT achieves state-of-the-art accuracy while delivering up to a $4.49 \times$ inference speed-up and halving the training memory footprint.

Our contributions can be summarized as follows:

- We identify and analyze inter-path adaptation, a critical manifestation of feature co-adaptation in residual binarization, where the intended error-compensation structure breaks down during Standard QAT, as parallel paths become functionally redundant.
- We propose RaBiT, a novel QAT framework that resolves inter-path adaptation by enforcing residual coupling on-the-fly. The mechanism inherently *halves the training memory footprint* and is stabilized by a robust function-aware initialization strategy to directly address the unstable dynamics of extreme QAT.
- We demonstrate that RaBiT achieves state-of-the-art accuracy at 2-bit precision, delivering up to a $4.49 \times$ inference speed-up while maintaining competitive performance against hardware-intensive VQ methods through matmul-free operations.

2. Related Works

The Shift to QAT in Extreme Quantization. Post-Training Quantization (PTQ) methods, such as GPTQ (Frantar et al., 2022) and AWQ (Lin et al., 2024), have proven to be highly successful for compressing large language models to 3- or 4-bit precision by focusing on weight approxima-

tion. However, these methods encounter substantial performance degradation at lower bit-widths (e.g., 2-bit) (Wang et al., 2023; Huang et al., 2024; Li et al., 2024), as the information loss inherent to coarse quantization cannot be mitigated solely by weight approximation. Consequently, more recent works target preserving global model functionality (Liu et al., 2025) via quantization-aware training (QAT) (Hubara et al., 2018; Krishnamoorthi, 2018). QAT integrates low-precision arithmetic simulations into the fine-tuning process, enabling parameter adaptation to the target bit-width constraints. Although the non-differentiable nature of quantization presents challenges—typically managed via the Straight-Through Estimator (STE) (Bengio et al., 2013)—modern frameworks for binary models have achieved stability by updating a latent full-precision weight via surrogate gradients (Wang et al., 2023; Xu et al., 2024; Jo et al., 2024; Lee et al., 2025). This work builds upon this methodology to address the specific complexities of residual binary architectures.

Co-adaptation in Residual Binary Architectures. To enhance the limited expressive capacity of single low-bit layers, residual binarization stacks multiple low-bit paths ($W \approx \sum_i \hat{W}_i$), thereby achieving higher effective precision while retaining matmul-free efficiency (Wang et al., 2024a). Nevertheless, this parallel structure is prone to **feature co-adaptation** (Hinton et al., 2012), where components learn redundant representations. This phenomenon previously motivated regularization techniques, such as Dropout (Srivastava et al., 2014).

Table 1. Detailed Decomposition of MSE Loss across Representative Layers of Llama2-7B. The table breaks down the total MSE into its core components. While the base error (C') and path amplitude ($2\sigma_1\sigma_2$) are comparable, RaBiT consistently generates a strong negative correlation, creating a significant loss-reducing bonus. In contrast, Standard QAT’s weak correlation provides a negligible benefit, demonstrating RaBiT’s structural advantage in error correction.

Layer	Method	Base Error (C')	Path Amp. ($2\sigma_1\sigma_2$)	Path Corr. (Corr)	Covariance (Amp. \times Corr)	Total MSE ($C' + \text{Cov.}$)
Layer 5 (Early)	Standard QAT	0.0019	0.0030	-0.0752	-0.0002	0.0017
	RaBiT (Ours)	0.0023	0.0028	-0.4961	-0.0014	0.0009
Layer 15 (Mid)	Standard QAT	0.0182	0.0214	-0.1240	-0.0026	0.0156
	RaBiT (Ours)	0.0163	0.0200	-0.3418	-0.0068	0.0094
Layer 25 (Late)	Standard QAT	0.0575	0.0728	-0.1279	-0.0093	0.0482
	RaBiT (Ours)	0.0609	0.0801	-0.3535	-0.0283	0.0327

We identify a critical form of feature co-adaptation in residual binarization, termed inter-path adaptation, wherein a shared QAT gradient compels parallel paths to acquire redundant features, compromising the error-compensation hierarchy. Unlike prior works that depend on suboptimal heuristics like path freezing (Bulat et al., 2024; Tran & Nguyen, 2025), which restrict the solution space, RaBiT resolves this issue structurally, facilitating true joint optimization while algorithmically enforcing the hierarchy.

3. Motivation

The goal of quantization-aware training (QAT) is to make a quantized student model, \mathbf{Y}_s , functionally mimic its full-precision teacher, \mathbf{Y}_t . This is typically achieved by optimizing an objective that combines the final task loss with an intermediate knowledge distillation loss, often formulated as the mean squared error (MSE) (Hinton et al., 2015; Liu et al., 2024). While our full training objective also includes the final KL divergence-based task loss, we initially focus our analysis on the MSE component for its analytical tractability. We formally prove that this error-decomposition logic and the optimality of RaBiT’s residual coupling extend rigorously to the KL divergence objective (see Appendix B). The additive structure of the MSE provides a clear window into how parallel paths interact. In a 2-bit residual architecture, the MSE between the teacher output y_t and the student output $y_s = y_1 + y_2$ can be decomposed. Using the Pearson correlation coefficient,¹ this decomposition is:

$$\text{MSE}(y_t, y_s) = \underbrace{(\mathbb{E}[y_t^2] + \mathbb{E}[y_1^2] + \mathbb{E}[y_2^2] - 2\mathbb{E}[y_t y_s])}_{C'} + \underbrace{2\sigma_1\sigma_2}_{\text{PathAmp.}} \cdot \underbrace{\text{Corr}(y_1, y_2)}_{\text{PathCorr.}}, \quad (1)$$

where C' represents the sum of correlation-independent er-

¹The relationship $\mathbb{E}[y_1 y_2] \approx \sigma_1 \sigma_2 \text{Corr}(y_1, y_2)$ relies on a zero-mean assumption for the path outputs. We empirically verify this, finding the omitted $\mathbb{E}[y_1] \mathbb{E}[y_2]$ term is less than 1% of the covariance term and thus negligible.

ror terms. This reveals a core principle: to minimize the MSE, the paths must be strongly *negatively correlated*. A negative correlation transforms the interaction term into a substantial bonus that actively reduces the total loss, signifying effective error-cancellation.

However, Standard QAT—which optimizes independent latent weights for parallel paths simultaneously via a shared gradient—structurally fails to achieve this. The shared global gradient induces **inter-path adaptation**, forcing both paths to learn redundant features instead of their intended compensatory roles (see Appendix A). To provide a concrete analysis, we decompose the MSE loss for representative layers of Llama2-7B, selected to show the characteristics across the early, middle, and late stages of the network, in Table 1.

The analysis in Table 1 is definitive. Across early, middle, and late stages of the network, the base error term C' and the path amplitude $2\sigma_1\sigma_2$ remain comparable between both methods. The critical difference lies in the correlation. Standard QAT yields a correlation close to zero, resulting in a negligible interaction term that fails to meaningfully reduce the total error. In contrast, RaBiT structurally enforces a strong negative correlation (e.g., -0.50 in layer 5) (see Appendix A). This transforms the interaction term into a significant loss-reducing bonus, systematically lowering the total MSE (see Appendix G). This principled enforcement of anti-correlation creates a more stable optimization landscape, leading to better generalization and superior performance.

4. Method

We introduce RaBiT, a novel QAT framework that prevents interference between the parallel paths of stacked binary architectures. To achieve this, RaBiT enforces a clear error-correction role for each path using a novel **coupled training** loop and stabilizes the process with a **function-aware initialization** strategy. An overview of the RaBiT training framework is illustrated in Figure 1.

4.1. The Residual Binarization Architecture

To efficiently achieve low-bit precision (*e.g.*, 2-bit), we adopt a residual architecture built upon highly efficient binary building blocks.

Binary Building Blocks. The fundamental component is the dual-scale binarization framework. We define the approximation of a weight matrix $\hat{\mathbf{W}}$ using a notation that highlights the underlying element-wise scaling operations:

$$\hat{\mathbf{W}} = \mathbf{g} \odot \mathbf{B} \odot \mathbf{h}. \quad (2)$$

Here, $(\hat{\mathbf{W}})_{ij}$ is computed as $g_i B_{ij} h_j$. $\mathbf{B} \in \{-1, +1\}^{d_{\text{out}} \times d_{\text{in}}}$ represents the binary core matrix, while $\mathbf{g} \in \mathbb{R}^{d_{\text{out}}}$ and $\mathbf{h} \in \mathbb{R}^{d_{\text{in}}}$ are full-precision, per-channel scaling vectors. This formulation facilitates matmul-free efficiency. For an input vector $\mathbf{x} \in \mathbb{R}^{d_{\text{in}}}$, the output $\mathbf{y} \in \mathbb{R}^{d_{\text{out}}}$ is computed as $\mathbf{y} = \mathbf{g} \odot (\mathbf{B}(\mathbf{h} \odot \mathbf{x}))$, implementable via additions and subtractions without costly matrix multiplications.

Multi-bit Approximation via Stacking. To increase representational capacity (*e.g.*, to 2-bit) while maintaining efficiency, $k = 2$ binary paths are stacked in parallel. The effective weight is the sum of binarized terms:

$$\hat{\mathbf{W}}^{(k)} = \sum_{i=1}^k \hat{\mathbf{W}}_i = \sum_{i=1}^k \mathbf{g}_i \odot \mathbf{B}_i \odot \mathbf{h}_i. \quad (3)$$

This architecture preserves matmul-free execution, as the forward pass accumulates outputs from each path.

4.2. Coupled Training for Co-Adaptation Mitigation

To prevent inter-path co-adaptation, RaBiT diverges from standard methods that train independent latent weights for each binary path. Instead, a **single shared full-precision (FP) weight** \mathbf{W}_{FP} is used as an anchor for the entire residual structure.

The Coupled Forward Pass. The mechanism relies on a dynamic forward pass. In a 2-bit configuration ($k = 2$), binary core matrices \mathbf{B}_1 and \mathbf{B}_2 are not explicitly stored. Rather, they are re-computed during each pass from the shared weight \mathbf{W}_{FP} (Figure 1a). This procedure algorithmically enforces an error-compensation hierarchy. While binary cores are dynamically derived, scaling vectors $\{\mathbf{g}_i, \mathbf{h}_i\}$ remain as independent learnable parameters to capture path-specific magnitudes. The forward pass consists of 3 steps:

1. **Path 1 Derivation:** The first binary core, \mathbf{B}_1 , is determined by directly binarizing the shared weight: $\mathbf{B}_1 = \text{sign}(\mathbf{W}_{\text{FP}})$. This core is combined with corresponding learnable scaling vectors, \mathbf{g}_1 and \mathbf{h}_1 , to reconstruct the first-path approximation $\hat{\mathbf{W}}_1 = \mathbf{g}_1 \odot \mathbf{B}_1 \odot \mathbf{h}_1$.

2. **Residual Calculation:** The residual error, \mathbf{R}_1 , is computed by subtracting the *reconstructed* first path from the shared weight: $\mathbf{R}_1 = \mathbf{W}_{\text{FP}} - \hat{\mathbf{W}}_1$.

3. **Path 2 Derivation:** The second binary core, \mathbf{B}_2 , is determined by binarizing this calculated residual error: $\mathbf{B}_2 = \text{sign}(\mathbf{R}_1)$. The final effective weight for the forward pass is the sum of the two reconstructed paths: $\hat{\mathbf{W}}^{(2)} = \hat{\mathbf{W}}_1 + (\mathbf{g}_2 \odot \mathbf{B}_2 \odot \mathbf{h}_2)$.

A critical distinction is made between dynamically deriving binary cores $\mathbf{B}_i := \text{sign}(\mathbf{R}_{i-1})$ and treating scaling vectors $\{\mathbf{g}_i, \mathbf{h}_i\}$ as independent parameters. This separation ensures computational feasibility and training stability. Recalculating optimal scales at every step—*e.g.*, via Singular Value Decomposition (SVD)—would impose prohibitive computational costs. By maintaining scales as learnable parameters, the optimizer applies state accumulation (*e.g.*, momentum) to fine-tune initialized values effectively (Section 4.3). Such data-adaptive tuning enables the error-compensation hierarchy to learn optimal magnitudes for each path.

Backward Pass and Parameter Updates. The backward pass facilitates stable parameter updates. Gradients from the loss \mathcal{L} propagate to both the independent scaling vectors $\{\mathbf{g}_i, \mathbf{h}_i\}$ and the shared weight \mathbf{W}_{FP} , as depicted in Figure 1c.

• **Gradient for the Shared Weight:** To update the single shared weight \mathbf{W}_{FP} , RaBiT employs an **effective-weight gradient**. This functions as a Straight-Through Estimator (STE) for the *entire coupled derivation process*. The gradient is computed with respect to the final effective weight $\hat{\mathbf{W}}^{(k)} = \sum_i \hat{\mathbf{W}}_i$ and is directly passed to update \mathbf{W}_{FP} . To ensure dimensional consistency for general cases ($d_{\text{in}} \neq d_{\text{out}}$), we formulate the update as:

$$\nabla_{\mathbf{W}_{\text{FP}}} \approx \nabla_{\hat{\mathbf{W}}^{(k)}} \mathcal{L} = \frac{\partial \mathcal{L}}{\partial \mathbf{Y}} \mathbf{X}^\top. \quad (4)$$

In this context, \mathcal{L} denotes the task loss, while $\mathbf{X} \in \mathbb{R}^{d_{\text{in}} \times N}$ and $\mathbf{Y} \in \mathbb{R}^{d_{\text{out}} \times N}$ represent the full input and output matrices for the mini-batch. By recomputing binary paths from the updated \mathbf{W}_{FP} at every step, the system forces each path to correct the most recent residual error, thereby preserving the error-compensation hierarchy.

• **Gradient for Learnable Scales:** The scaling vectors $\{\mathbf{g}_i, \mathbf{h}_i\}$ function as standard learnable parameters and receive gradients via the chain rule. For a mini-batch of size N , gradients are accumulated over each sample while

treating the dynamic binary cores (\mathbf{B}_i) as constants:

$$\begin{aligned}\nabla_{\mathbf{g}_i} &= \sum_{n=1}^N \Delta_n \odot (\mathbf{B}_i(\mathbf{h}_i \odot \mathbf{x}_n)), \\ \nabla_{\mathbf{h}_i} &= \sum_{n=1}^N (\mathbf{B}_i^\top (\Delta_n \odot \mathbf{g}_i)) \odot \mathbf{x}_n.\end{aligned}\quad (5)$$

Here, \mathbf{x}_n denotes the input vector corresponding to the n -th column of \mathbf{X} , and $\Delta_n = (\partial \mathcal{L} / \partial \mathbf{y}_n)$ represents the upstream gradient from the layer's output vector \mathbf{y}_n .

During inference, the final binary cores $\{\mathbf{B}_i\}$ are derived from the trained \mathbf{W}_{FP} and frozen, allowing \mathbf{W}_{FP} to be discarded. This yields a highly efficient architecture where independent paths execute in a fully parallel, matmul-free manner. Furthermore, the single-weight design reduces memory usage for optimizer states by 50%, addressing a primary bottleneck in LLM fine-tuning. The complete training procedure is detailed in Algorithm 2.

4.3. Stable Initialization for Functional Preservation

Quantization-aware training (QAT) in the 2-bit regime is sensitive to initialization, often trapping models in suboptimal minima (Nagel et al., 2020; Liu et al., 2024). To address this, we implement a two-stage initialization process designed to preserve model *functionality* rather than simply approximating weight values.

1. Iterative Residual SVID. The primary objective is to identify binary paths that jointly approximate the target matrix. Standard greedy decomposition is suboptimal as early choices irreversibly bias subsequent paths. Therefore, we employ **Iterative Residual Sign-Value-Independent Decomposition (SVID)**, a Gauss-Seidel style iteration facilitating path co-adaptation. The process refines scales $\{\mathbf{g}_i, \mathbf{h}_i\}$ and binary cores $\{\mathbf{B}_i\}$ for each path $i = 1, \dots, k$ over iterations $t = 1, \dots, T$ as follows:

$$\begin{cases} \mathbf{R}_i^{(t)} := \mathbf{W}_{\text{FP}} - \sum_{j < i} \hat{\mathbf{W}}_j^{(t)} \\ \quad - \sum_{j > i} \hat{\mathbf{W}}_j^{(t-1)}, \\ \mathbf{B}_i^{(t)}, \mathbf{g}_i^{(t)}, \mathbf{h}_i^{(t)} := \text{SVID}(\mathbf{R}_i^{(t)}), \\ \hat{\mathbf{W}}_i^{(t)} := \mathbf{g}_i^{(t)} \odot \mathbf{B}_i^{(t)} \odot \mathbf{h}_i^{(t)}. \end{cases} \quad (6)$$

SVID(\cdot) (Xu et al., 2024) extracts optimal per-channel scales via rank-1 SVD approximation on the magnitudes. In practice, this iterative process is applied to a preconditioned target matrix \mathbf{W}' rather than the raw weights \mathbf{W}_{FP} .

2. I/O Channel Importance-Scaled Preconditioning. To focus decomposition on functionally critical weight components, the raw weights \mathbf{W}_{FP} are not used directly. Drawing on recent methods for functional saliency preservation (Boža & Macko, 2025), the matrix is preconditioned

to generate a target \mathbf{W}' . Using a calibration dataset, input activation magnitudes (\mathbf{s}_{in}) and output gradient magnitudes (\mathbf{s}_{out}) are computed as the maximum absolute values and normalized to re-weight the full-precision matrix:

$$\mathbf{W}' = \mathbf{s}_{\text{out}}^{\alpha_{\text{out}}} \odot \mathbf{W}_{\text{FP}} \odot \mathbf{s}_{\text{in}}^{\alpha_{\text{in}}}. \quad (7)$$

Following Iterative Residual SVID, the resulting scales are mapped back to the original domain: $\mathbf{g}_i = \mathbf{s}_{\text{out}}^{-\alpha_{\text{out}}} \odot \mathbf{g}'_i$ and $\mathbf{h}_i = \mathbf{s}_{\text{in}}^{-\alpha_{\text{in}}} \odot \mathbf{h}'_i$. This approach reduces initial task loss and stabilizes the QAT startup phase (see Algorithm 1, Table 7, and Figure 5).

5. Experiments

5.1. Experimental Settings

Setup. The RaBiT framework is evaluated using the Llama2, Llama3, and Gemma3 model families (Touvron et al., 2023; Grattafiori et al., 2024; Team et al., 2025). For quantization-aware training (QAT), a calibration dataset of 200 million tokens is derived from the combined WikiText-2 and C4 datasets (Jo et al., 2024). Performance assessment relies primarily on perplexity (PPL) calculated on validation sets with a context length of 4096.

Evaluation Benchmarks. We report the average zero-shot accuracy (QA Avg.) across five standard reasoning benchmarks, including HellaSwag, PIQA, WinoGrande, ARC-e and ARC-c (Zellers et al., 2019; Bisk et al., 2020; Sakaguchi et al., 2021; Clark et al., 2018). Detailed breakdowns for these standard benchmarks are provided in Appendix D. Furthermore, to test the model's robustness on harder tasks involving complex reasoning and instruction following, we include evaluation on Big Bench Hard (BBH), GPQA, MMLU-Pro, and IFEval (Suzgun et al., 2023; Rein et al., 2024; Wang et al., 2024b; Zhou et al., 2023). These challenging benchmarks serve to highlight the functional preservation of the quantized models beyond basic language modeling metrics.

Training Details. The training process uses a QAT framework integrated with Knowledge Distillation (KD) (Hinton et al., 2015; Liu et al., 2024), employing the full-precision model as the teacher. The objective function combines the Kullback–Leibler (KL) divergence loss on output logits with intermediate mean squared error (MSE) losses: $\mathcal{L}_{\text{total}} = \mathcal{L}_{\text{kl}} + \gamma \sum_i \mathcal{L}_{\text{inter},i}$. We set $\gamma = 100$ for Llama models and $\gamma = 0$ for Gemma3 to mitigate instability caused by large activation ranges (Han & Han, 2025). Models are trained for 6 epochs using the Muon optimizer (Jordan et al., 2024) and our proposed function-aware initialization. We provide comprehensive hyperparameter configurations in Appendix F.

Table 2. Comparison with state-of-the-art 2-3-bit methods on Llama models. We report perplexity (PPL \downarrow) and zero-shot QA Average (\uparrow). For the 2-bit results, the best and runner-up are marked in **bold** and underlined, respectively. RaBiT achieves state-of-the-art (SOTA) performance on Llama2-7B and Llama3-8B, while showing highly competitive results on Llama2-13B.

Methods	Llama2-7B				Llama2-13B				Llama3-8B			
	Bit	Wiki2 \downarrow	C4 \downarrow	QA Avg \uparrow	Bit	Wiki2 \downarrow	C4 \downarrow	QA Avg \uparrow	Bit	Wiki2 \downarrow	C4 \downarrow	QA Avg \uparrow
Baseline	16	5.12	6.63	62.26	16	4.57	6.05	65.46	16	5.75	8.32	68.66
GPTQ	2.1	50.75	36.76	39.16	2.1	43.84	23.07	43.72	2	1.21e3	4.97e2	35.59
EfficientQAT	2.1	6.42	8.34	57.75	2.1	5.58	7.40	62.07	2.1	8.75	12.09	60.63
AQLM	2.3	6.29	8.56	58.57	2.2	5.41	7.20	61.58	2.3	7.23	10.32	64.12
QuIP#	2	6.19	8.16	58.23	2	5.35	7.20	61.96	2	8.70	12.04	63.89
QTIP	2	<u>5.86</u>	<u>7.73</u>	<u>58.97</u>	2	5.11	6.85	62.92	2	<u>7.52</u>	<u>10.76</u>	<u>63.88</u>
BitStack	3	6.91	9.10	56.54	3	5.90	7.86	61.06	3	12.38	17.51	58.41
	2	29.97	34.91	40.12	2	67.98	72.60	39.38	2	2.75e3	1.93e3	36.21
DB-LLM	2	7.23	9.62	55.12	2	6.19	8.38	59.41	2	12.08	16.80	50.92
MBOK	3	6.13	8.13	54.63	3	5.14	6.94	62.73	3	7.81	11.29	61.08
	2	6.99	9.38	53.63	2	5.76	7.89	60.58	2	10.74	14.61	54.41
DBF	2.3	5.81	7.69	59.84	2.3	5.15	6.85	62.53	2.3	7.22	10.34	64.84
	2	6.10	8.05	58.42	2	5.33	7.13	61.53	2	7.78	10.99	62.90
RaBiT (Ours)	3	5.36	7.06	63.05	3	4.84	6.51	64.09	3	6.58	9.54	65.61
	2	5.78	7.64	61.51	2	<u>5.15</u>	<u>6.95</u>	<u>62.10</u>	2	7.34	10.52	64.13

Table 3. Comparison with state-of-the-art 2-bit methods on Gemma3 models. We report perplexity (PPL \downarrow) and zero-shot QA Average (\uparrow). The context length is 4096. RaBiT consistently achieves SOTA or highly competitive performance, demonstrating its robustness across diverse model architectures.

Methods	Gemma3-1B				Gemma3-4B				Gemma3-12B			
	Bit	Wiki2 \downarrow	C4 \downarrow	QA Avg \uparrow	Bit	Wiki2 \downarrow	C4 \downarrow	QA Avg \uparrow	Bit	Wiki2 \downarrow	C4 \downarrow	QA Avg \uparrow
Baseline	16	9.80	13.69	57.82	16	6.88	10.44	67.60	16	5.50	9.28	73.45
DBF	2	13.28	17.57	51.98	2	8.72	12.71	60.91	2	6.97	10.60	68.37
QTIP	2	13.14	17.36	50.30	2	8.31	12.21	63.47	2	6.65	10.25	69.69
RaBiT (Ours)	2	11.27	15.54	53.18	2	8.09	11.91	62.21	2	6.66	10.18	68.85

Baselines. We compare RaBiT against a broad spectrum of state-of-the-art 2- to 3-bit quantization methods. These include: (1) standard post-training quantization methods such as GPTQ and EfficientQAT (Frantar et al., 2022; Chen et al., 2025); (2) high-accuracy Vector Quantization (VQ) approaches including AQLM, QuIP#, and QTIP (Egiazarian et al., 2024; Tseng et al., 2024a;b), which typically incur high hardware overhead; and (3) hardware-efficient binary and residual methods such as BitStack, DB-LLM, MBOK, and DBF (Wang et al., 2024a; Chen et al., 2024; Tran & Nguyen, 2025; Boža & Macko, 2025)², which serve as the most direct architectural comparisons.

5.2. Main Results

The empirical results, summarized in Tables 2 to 4, demonstrate that RaBiT consistently redefines the state-of-the-

²We rely on our re-implementation for DB-LLM and MBOK.

art for 2-bit quantization, exhibiting superior performance across all tested model architectures and datasets.

Dominance over Hardware-Efficient Methods. RaBiT significantly outperforms existing matmul-free binary and residual methods, highlighting the efficacy of the proposed optimization strategy. On the Llama2-7B benchmark, RaBiT achieves a WikiText-2 perplexity (PPL) of 5.78. This represents a substantial improvement over direct competitors such as MBOK (6.99 PPL) and DBF (6.10 PPL). The performance gap becomes even more pronounced on larger models and more complex datasets, which underscores the severe performance penalty incurred by the inter-path adaptation issues that prior methods fail to address. Notably, we observed that methods lacking our principled coupled design, such as BitStack, suffer from catastrophic instability on newer architectures like Llama3-8B (degrading to 2.75e3 PPL), whereas RaBiT successfully maintains robust convergence and high fidelity.

Table 4. Zero-shot evaluation on challenging benchmarks. We report BBH, GPQA, MMLU-Pro, and IFEval results for Llama2-13B and Llama3-8B.

Methods	Llama2-13B			Llama3-8B		
	Baseline	QTIP	RaBiT	Baseline	QTIP	RaBiT
Bit	16	2	2	16	2	2
BBH	40.99	33.36	37.72	45.84	36.27	36.78
GPQA	27.45	25.75	26.77	30.85	24.56	28.62
MMLU-Pro	24.81	16.69	19.44	14.91	19.24	19.65
IFEval	23.83	25.74	24.63	32.51	15.60	15.42
Average	29.27	25.38	27.14	31.03	23.92	25.12

Achieving VQ-Level Accuracy with Binary Efficiency.

Perhaps most impressively, RaBiT effectively closes the gap with—and frequently surpasses—hardware-intensive Vector Quantization (VQ) methods, thereby resolving the historical trade-off between accuracy and efficiency. On Llama2-7B, RaBiT’s perplexity of 5.78 edges out the leading VQ method, QTIP (5.86 PPL). This trend holds for downstream reasoning tasks as well; RaBiT achieves a 61.51% average zero-shot accuracy on Llama2-7B, surpassing QTIP’s 58.97% and demonstrating superior functional preservation.

This robustness is further corroborated by results on Llama3-8B, where RaBiT maintains strong performance (7.34 PPL) while other VQ methods like QuIP# suffer from severe degradation (8.70 PPL). As shown in Table 3, this advantage generalizes beyond the Llama family. On the Gemma3 suite (1B/4B/12B), RaBiT consistently delivers competitive perplexity and robust zero-shot QA accuracy.

Performance on Harder Tasks. To further validate the model’s capabilities in complex scenarios, we evaluated performance on challenging benchmarks including BBH, GPQA, MMLU-Pro, and IFEval. As presented in Table 4, RaBiT outperforms QTIP on average (27.14 vs. 25.38 on Llama2-13B) and retains substantially more capability relative to the full-precision baseline than prior quantization techniques. This indicates that RaBiT’s coupled training strategy preserves the delicate internal representations required for advanced reasoning and instruction following, which are often lost in standard binary quantization.

5.3. Ablation Studies

5.3.1. COMPONENT-WISE CONTRIBUTION ANALYSIS

We performed an ablation study to analyze the contributions of RaBiT’s core components Coupled QAT, Iterative SVID (**I**), and I/O Channel Importance-Scaled Preconditioning (**S**), with results in Table 5. The analysis clearly shows that **Coupled QAT** is the most critical performance factor. Simply switching from Standard QAT (6.55 PPL)

Table 5. Ablation on RaBiT (Llama2-7B PPL). The analysis isolates the impact of Iterative Residual SVID (**I**) and I/O Channel Importance-Scaled Preconditioning (**S**).

Training Method	I	S	WikiText-2 ↓
Standard QAT	✓		6.55
		✓	6.21
	✓	✓	6.31
Coupled QAT (RaBiT)	✓		5.84
		✓	5.80
	✓	✓	5.81
			5.78

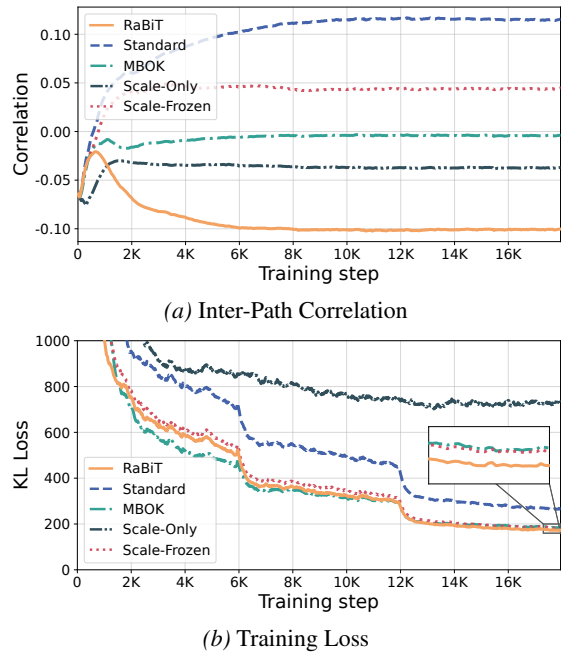


Figure 2. Visualization of Coupled Training Dynamics. (a) **Inter-Path Correlation:** RaBiT enforces a negative inter-path correlation, indicating effective error-correction, whereas Standard QAT leads to positive correlation (co-adaptation). (b) **Training Loss:** This structural advantage directly translates to a lower and more stable training loss for RaBiT, demonstrating its superior optimization path.

to Coupled QAT reduces the perplexity to 5.84, confirming that resolving inter-path adaptation yields the largest gain. Our initialization methods (**I** and **S**) provide further essential improvements. While they offer a significant boost to the baseline Standard QAT, their role within the powerful Coupled QAT framework is to provide the final, crucial fine-tuning needed to reach the optimal 5.78 PPL. This synergy between a robust training method and a function-aware initialization is key to state-of-the-art performance of RaBiT.

Table 6. Inference Performance Analysis on NVIDIA RTX 4090. Kernel latency for key Llama2-7B/13B layers and Llama2-7B decoding throughput for a 256-token generation. RaBiT shows superior efficiency at both the kernel and system levels.

Method	Bit	Kernel-Level Latency (μs) \downarrow				End-to-End Decoding Throughput (tok/s) \uparrow
		4096 \times 4096 (q_proj, 7B)	11008 \times 4096 (gate_proj, 7B)	5120 \times 5120 (q_proj, 13B)	13824 \times 5120 (gate_proj, 13B)	
FP16	16	17.15 (1.00 \times)	70.37 (1.00 \times)	17.85 (1.00 \times)	122.90 (1.00 \times)	64.96 (1.00 \times)
DBF	2.3	12.66 (1.35 \times)	28.43 (2.48 \times)	14.72 (1.21 \times)	31.87 (3.86 \times)	157.66 (2.43 \times)
	2	11.47 (1.50 \times)	20.90 (3.37 \times)	14.08 (1.27 \times)	29.58 (4.15 \times)	175.21 (2.70 \times)
QTIP	3	24.04 (0.71 \times)	37.08 (1.90 \times)	36.22 (0.49 \times)	49.97 (2.46 \times)	153.59 (2.36 \times)
	2	23.40 (0.73 \times)	42.40 (1.66 \times)	37.46 (0.48 \times)	59.22 (2.08 \times)	171.74 (2.64 \times)
RaBiT (Ours)	3	8.15 (2.10\times)	17.13 (4.11\times)	9.90 (1.80\times)	22.36 (5.50\times)	191.63 (2.95\times)
	2	7.72 (2.22\times)	15.71 (4.48\times)	8.33 (2.14\times)	17.50 (7.02\times)	291.88 (4.49\times)

5.3.2. ANALYSIS OF COUPLED TRAINING DYNAMICS

To empirically validate that coupled training resolves co-adaptation, we conducted a controlled experiment comparing RaBiT to four variants: (1) Standard QAT (independent latent weights), (2) MBOK (frozen primary binary core, mimicking the path-freezing heuristic of [Tran & Nguyen \(2025\)](#) within our training loop), (3) Scale-only (frozen binary cores), and (4) Scale-frozen (RaBiT with frozen scales). To strictly isolate architectural dynamics from optimizer-specific effects, we standardize the initialization and optimizer (Muon) across all variants.

Figure 2 reveals the resulting training dynamics. As theorized, RaBiT successfully maintains a stable negative inter-path correlation, enforcing the error-correction hierarchy (Figure 2a). In contrast, Standard QAT develops a strong positive correlation, confirming that a shared global gradient induces harmful redundancy. The constrained variants (MBOK, Scale-frozen) fail to establish a strong anti-correlation, limiting their optimization potential. This structural advantage directly translates to model functionality, as shown by the training loss curves (Figure 2b). RaBiT achieves the lowest and most stable loss, while the co-adaptation in Standard QAT and the incomplete optimization of the other variants lead to significantly higher loss. This analysis confirms that sequential optimization of all parameters algorithmically prevents co-adaptation and results in its superior performance.

5.4. Inference Performance

RaBiT not only achieves state-of-the-art accuracy but also delivers exceptional inference speed by leveraging its parallelizable matmul-free binary architecture. As shown in Table 6, 2-bit RaBiT achieves a 4.49 \times speed-up in end-to-end decoding throughput over the FP16 baseline, on an NVIDIA RTX 4090.

This performance gain stems from two key advantages. First, the 8 \times reduction in model size (2-bit vs. 16-bit) dra-

matically lowers memory bandwidth requirements, which is the primary bottleneck in the autoregressive decoding phase. Second, unlike VQ methods, RaBiT avoids hardware-unfriendly overheads like lookup tables or rotations. Its simple architecture of additions and element-wise scaling translates to higher hardware utilization. This is evident in our kernel-level benchmarks, where RaBiT’s specialized kernels exhibit consistently lower latency than both the FP16 baseline and QTIP’s VQ kernels. By eliminating computational complexity, RaBiT ensures that theoretical memory savings translate directly into real-world speed, delivering a solution that is both accurate and genuinely efficient. Further details on our kernel design and additional performance benchmarks are provided in Appendix E.1 and Appendix E.2, respectively.

6. Conclusion

This study addresses the trade-off between accuracy and hardware efficiency in 2-bit large language model (LLM) quantization through the introduction of RaBiT. We identified inter-path adaptation as a primary bottleneck that compromises the error-compensation structure in residual binarization. To mitigate this, the proposed framework employs on-the-fly residual coupling, a mechanism that prevents structural breakdown during training and ensures that the expressive capacity of the model is effectively used. Furthermore, to address the instability inherent in extreme quantization, we introduced a function-aware initialization strategy that facilitates stable convergence. Experimental results indicate that RaBiT achieves state-of-the-art performance at 2-bit precision, outperforming both existing binary methods and hardware-intensive Vector Quantization (VQ) approaches. By establishing these capabilities, this work offers a viable pathway for the efficient deployment of high-performance low-bit LLMs and serves as a scalable foundation for future research.

Impact Statement

This paper presents RaBiT, a framework for the extreme 2-bit quantization of LLMs. By drastically reducing computational requirements, our work is environmentally friendly and democratizes access, enabling high-performance models to run on consumer hardware (*e.g.*, RTX 4090). This efficiency facilitates local deployment, thereby enhancing user privacy and data sovereignty compared to cloud-based solutions. However, such accessibility also introduces dual-use risks by potentially enabling malicious applications outside controlled environments. Additionally, while our method preserves general capabilities, the specific effects of extreme compression on safety alignment remain an important area for future investigation.

References

Bengio, Y., Léonard, N., and Courville, A. Estimating or Propagating Gradients Through Stochastic Neurons for Conditional Computation. *arXiv preprint arXiv:1308.3432*, 2013.

Bisk, Y., Zellers, R., Gao, J., Choi, Y., et al. PIQA: Reasoning About Physical Commonsense in Natural Language. In *Proceedings of the AAAI conference on artificial intelligence*, volume 34, pp. 7432–7439, 2020.

Boža, V. and Macko, V. Addition Is Almost All You Need: Compressing Neural Networks with Double Binary Factorization. *arXiv preprint arXiv:2505.11076*, 2025.

Bulat, A., Ouali, Y., and Tzimiropoulos, G. QBB: Quantization with Binary Bases for LLMs. *Advances in Neural Information Processing Systems*, 37:3209–3228, 2024.

Chen, H., Lv, C., Ding, L., Qin, H., Zhou, X., Ding, Y., Liu, X., Zhang, M., Guo, J., Liu, X., et al. DB-LLM: Accurate Dual-Binarization for Efficient LLMs. *arXiv preprint arXiv:2402.11960*, 2024.

Chen, M., Shao, W., Xu, P., Wang, J., Gao, P., Zhang, K., and Luo, P. EfficientQAT: Efficient Quantization-Aware Training for Large Language Models. In *Proceedings of the 63rd Annual Meeting of the Association for Computational Linguistics (Volume 1: Long Papers)*, pp. 10081–10100, 2025.

Clark, P., Cowhey, I., Etzioni, O., Khot, T., Sabharwal, A., Schoenick, C., and Tafjord, O. Think You Have Solved Question Answering? Try ARC, the AI2 Reasoning Challenge. *arXiv preprint arXiv:1803.05457*, 2018.

Egiazarian, V., Panferov, A., Kuznedelev, D., Frantar, E., Babenko, A., and Alistarh, D. Extreme Compression of Large Language Models via Additive Quantization. *arXiv preprint arXiv:2401.06118*, 2024.

Frantar, E., Ashkboos, S., Hoefer, T., and Alistarh, D. GPTQ: Accurate Post-Training Quantization for Generative Pre-trained Transformers. *arXiv preprint arXiv:2210.17323*, 2022.

Grattafiori, A., Dubey, A., Jauhri, A., Pandey, A., Kadian, A., Al-Dahle, A., Letman, A., Mathur, A., Schelten, A., Vaughan, A., et al. The Llama 3 Herd of Models. *arXiv preprint arXiv:2407.21783*, 2024.

Han, D. and Han, M. Fine-tune gemma 3 with unsloth, March 2025. URL <https://unsloth.ai/blog/gemma3>. Accessed: 2026-01-29.

Hinton, G., Vinyals, O., and Dean, J. Distilling the Knowledge in a Neural Network. *arXiv preprint arXiv:1503.02531*, 2015.

Hinton, G. E., Srivastava, N., Krizhevsky, A., Sutskever, I., and Salakhutdinov, R. R. Improving Neural Networks by Preventing Co-Adaptation of Feature Detectors. *arXiv preprint arXiv:1207.0580*, 2012.

Huang, W., Liu, Y., Qin, H., Li, Y., Zhang, S., Liu, X., Magno, M., and Qi, X. BiLLM: Pushing the Limit of Post-Training Quantization for LLMs. *arXiv preprint arXiv:2402.04291*, 2024.

Hubara, I., Courbariaux, M., Soudry, D., El-Yaniv, R., and Bengio, Y. Quantized Neural Networks: Training Neural Networks with Low Precision Weights and Activations. *Journal of Machine Learning Research*, 18(187):1–30, 2018.

Jo, D., Kim, T., Kim, Y., et al. Mixture of Scales: Memory-Efficient Token-Adaptive Binarization for Large Language Models. *Advances in Neural Information Processing Systems*, 37:137474–137494, 2024.

Jordan, K., Jin, Y., Boza, V., Jiacheng, Y., Cesista, F., Newhouse, L., and Bernstein, J. Muon: An Optimizer for Hidden Layers in Neural Networks, 2024. URL <https://kellerjordan.github.io/posts/muon/>.

Kim, T., Oh, J., Kim, N. Y., Cho, S., and Yun, S.-Y. Comparing Kullback-Leibler Divergence and Mean Squared Error Loss in Knowledge Distillation. In *Proceedings of the Thirtieth International Joint Conference on Artificial Intelligence*. International Joint Conferences on Artificial Intelligence Organization, 2021.

Krishnamoorthi, R. Quantizing Deep Convolutional Networks for Efficient Inference: A Whitepaper. *arXiv preprint arXiv:1806.08342*, 2018.

Kwon, W., Li, Z., Zhuang, S., Sheng, Y., Zheng, L., Yu, C. H., Gonzalez, J. E., Zhang, H., and Stoica, I. Efficient Memory Management for Large Language Model

Serving with PagedAttention. In *Proceedings of the ACM SIGOPS 29th Symposium on Operating Systems Principles*, 2023.

Lee, B., Kim, D., You, Y., and Kim, Y. LittleBit: Ultra Low-Bit Quantization via Latent Factorization. *arXiv preprint arXiv:2506.13771*, 2025.

Li, Z., Yan, X., Zhang, T., Qin, H., Xie, D., Tian, J., Kong, L., Zhang, Y., Yang, X., et al. ARB-LLM: Alternating Refined Binarizations for Large Language Models. *arXiv preprint arXiv:2410.03129*, 2024.

Lin, J., Tang, J., Tang, H., Yang, S., Chen, W.-M., Wang, W.-C., Xiao, G., Dang, X., Gan, C., and Han, S. AWQ: Activation-Aware Weight Quantization for On-Device LLM Compression and Acceleration. *Proceedings of machine learning and systems*, 6:87–100, 2024.

Liu, Z., Oguz, B., Zhao, C., Chang, E., Stock, P., Mehdad, Y., Shi, Y., Krishnamoorthi, R., and Chandra, V. LLM-QAT: Data-Free Quantization Aware Training for Large Language Models. In *Findings of the Association for Computational Linguistics: ACL 2024*, pp. 467–484, 2024.

Liu, Z., Zhao, C., Huang, H., Chen, S., Zhang, J., Zhao, J., Roy, S., Jin, L., Xiong, Y., Shi, Y., et al. ParetoQ: Scaling Laws in Extremely Low-Bit LLM Quantization. *arXiv preprint arXiv:2502.02631*, 2025.

Nagel, M., Amjad, R. A., Van Baalen, M., Louizos, C., and Blankevoort, T. Up or Down? Adaptive Rounding for Post-Training Quantization. In *International Conference on Machine Learning*, pp. 7197–7206. PMLR, 2020.

Rein, D., Hou, B. L., Stickland, A. C., Petty, J., Pang, R. Y., Dirani, J., Michael, J., and Bowman, S. R. GPQA: A Graduate-Level Google-Proof Q&A Benchmark. In *First Conference on Language Modeling*, 2024.

Sakaguchi, K., Bras, R. L., Bhagavatula, C., and Choi, Y. WinoGrande: An Adversarial Winograd Schema Challenge at Scale. *Communications of the ACM*, 64(9):99–106, 2021.

Srivastava, N., Hinton, G., Krizhevsky, A., Sutskever, I., and Salakhutdinov, R. Dropout: A Simple Way to Prevent Neural Networks from Overfitting. *The journal of machine learning research*, 15(1):1929–1958, 2014.

Suzgun, M., Scales, N., Schärli, N., Gehrmann, S., Tay, Y., Chung, H. W., Chowdhery, A., Le, Q., Chi, E., Zhou, D., et al. Challenging Big-Bench Tasks and Whether Chain-of-Thought Can Solve Them. In *Findings of the Association for Computational Linguistics: ACL 2023*, pp. 13003–13051, 2023.

Team, G., Kamath, A., Ferret, J., Pathak, S., Vieillard, N., Merhej, R., Perrin, S., Matejovicova, T., Ramé, A., Rivière, M., et al. Gemma 3 Technical Report. *arXiv preprint arXiv:2503.19786*, 2025.

Touvron, H., Martin, L., Stone, K., Albert, P., Almahairi, A., Babaei, Y., Bashlykov, N., Batra, S., Bhargava, P., Bhosale, S., et al. Llama 2: Open Foundation and Fine-Tuned Chat Models. *arXiv preprint arXiv:2307.09288*, 2023.

Tran, B.-H. and Nguyen, V. M. Highly Efficient and Effective LLMs with Multi-Boolean Architectures. *arXiv preprint arXiv:2505.22811*, 2025.

Tseng, A., Chee, J., Sun, Q., Kuleshov, V., and De Sa, C. QuIP#: Even Better LLM Quantization with Hadamard Incoherence and Lattice Codebooks. *arXiv preprint arXiv:2402.04396*, 2024a.

Tseng, A., Sun, Q., Hou, D., and De Sa, C. M. QTIP: Quantization with Trellises and Incoherence Processing. *Advances in Neural Information Processing Systems*, 37: 59597–59620, 2024b.

Wang, H., Ma, S., Dong, L., Huang, S., Wang, H., Ma, L., Yang, F., Wang, R., Wu, Y., and Wei, F. BitNet: Scaling 1-Bit Transformers for Large Language Models. *arXiv preprint arXiv:2310.11453*, 2023.

Wang, X., Wang, P., Wang, B., Zhang, D., Zhou, Y., and Qiu, X. BitStack: Any-Size Compression of Large Language Models in Variable Memory Environments. *arXiv preprint arXiv:2410.23918*, 2024a.

Wang, Y., Ma, X., Zhang, G., Ni, Y., Chandra, A., Guo, S., Ren, W., Arulraj, A., He, X., Jiang, Z., et al. MMLU-Pro: A More Robust and Challenging Multi-Task Language Understanding Benchmark. *Advances in Neural Information Processing Systems*, 37:95266–95290, 2024b.

Xu, Y., Han, X., Yang, Z., Wang, S., Zhu, Q., Liu, Z., Liu, W., and Che, W. OneBit: Towards Extremely Low-Bit Large Language Models. *Advances in Neural Information Processing Systems*, 37:66357–66382, 2024.

Zellers, R., Holtzman, A., Bisk, Y., Farhadi, A., and Choi, Y. HellaSwag: Can a Machine Really Finish Your Sentence? *arXiv preprint arXiv:1905.07830*, 2019.

Zhang, F., Liu, Y., Li, W., Lv, J., Wang, X., and Bai, Q. Towards Superior Quantization Accuracy: A Layer-Sensitive Approach. *arXiv preprint arXiv:2503.06518*, 2025.

Zhang, Y., Dong, Y., and Kawaguchi, K. Investigating Layer Importance in Large Language Models. *arXiv preprint arXiv:2409.14381*, 2024.

Zheng, L., Yin, L., Xie, Z., Sun, C. L., Huang, J., Yu, C. H.,
Cao, S., Kozyrakis, C., Stoica, I., Gonzalez, J. E., et al.
SGLang: Efficient Execution of Structured Language
Model Programs. *Advances in Neural Information Pro-
cessing Systems*, 37:62557–62583, 2024.

Zhou, J., Lu, T., Mishra, S., Brahma, S., Basu, S., Luan,
Y., Zhou, D., and Hou, L. Instruction-Following Eval-
uation for Large Language Models. *arXiv preprint
arXiv:2311.07911*, 2023.

A. Mathematical Analysis of Training Dynamics

This section provides a mathematical analysis of the training dynamics for residual binary architectures. We demonstrate why Standard QAT is prone to **inter-path adaptation**, where paths become redundant. In contrast, we show how RaBiT's coupled training mechanism structurally enforces an **error-correcting hierarchy** and is superior to other heuristic solutions.

Proposition 1 (Inter-Path Adaptation in Standard QAT). *In a Standard QAT scheme where two paths $(\hat{\mathbf{W}}_1, \hat{\mathbf{W}}_2)$ are updated from their respective latent weights $(\mathbf{W}_1, \mathbf{W}_2)$ using a shared global gradient $\mathbf{G} = \nabla_{\hat{\mathbf{W}}_1 + \hat{\mathbf{W}}_2} \mathcal{L}$, the paths have a persistent tendency to become positively correlated, leading to redundancy.*

Proof. Let the latent weights be \mathbf{W}_1 and \mathbf{W}_2 . After a single update step with learning rate η and shared gradient \mathbf{G} , the new weights are \mathbf{W}'_1 and \mathbf{W}'_2 :

$$\mathbf{W}'_1 := \mathbf{W}_1 - \eta \mathbf{G} \quad \text{and} \quad \mathbf{W}'_2 := \mathbf{W}_2 - \eta \mathbf{G}$$

The change in the Frobenius inner product between the weights, which reflects their correlation, is:

$$\Delta_{\langle \cdot, \cdot \rangle} := \langle \mathbf{W}'_1, \mathbf{W}'_2 \rangle_F - \langle \mathbf{W}_1, \mathbf{W}_2 \rangle_F$$

Expanding this gives:

$$\Delta_{\langle \cdot, \cdot \rangle} = -\eta (\langle \mathbf{W}_1, \mathbf{G} \rangle_F + \langle \mathbf{W}_2, \mathbf{G} \rangle_F) + \eta^2 \|\mathbf{G}\|_F^2$$

While the linear terms depend on the alignment between the current weights and the gradient, the quadratic term $\eta^2 \|\mathbf{G}\|_F^2$ is **always non-negative**. This term acts as a systematic force, constantly pushing the two paths in the same direction defined by the global gradient \mathbf{G} . This dynamic, the underlying mechanism of **inter-path adaptation**, compels both paths to learn redundant, dominant features in order to minimize the global loss. This ultimately leads to a breakdown of the intended residual hierarchy and compromises the model's expressive capacity. \square

Proposition 2 (Structurally Enforced Error Correction in RaBiT). *RaBiT's coupled training mechanism resolves the redundancy drift by fundamentally changing the optimization objective. Instead of independent updates, RaBiT's on-the-fly derivation structurally forces the second path $(\hat{\mathbf{W}}_2)$ to align with the true residual of the first path ($\mathbf{R}_1 = \mathbf{W}_{\text{FP}} - \hat{\mathbf{W}}_1$), thereby enforcing an error-correcting relationship.*

Analysis. The optimization objectives of the two paths are implicitly different in RaBiT versus the naïve approach.

- **Standard QAT Objective:** Both paths are driven by the same structurally-agnostic global gradient \mathbf{G} . Their implicit goal is to align with \mathbf{G} to reduce the global loss. Since both $\hat{\mathbf{W}}_1$ and $\hat{\mathbf{W}}_2$ are incentivized to align with the same vector \mathbf{G} , they inevitably learn to align with each other, leading to redundancy as shown in Proposition 1.

$$\hat{\mathbf{W}}_1 \propto \mathbf{G} \quad \text{and} \quad \hat{\mathbf{W}}_2 \propto \mathbf{G} \implies \langle \hat{\mathbf{W}}_1, \hat{\mathbf{W}}_2 \rangle_F > 0$$

- **RaBiT's Enforced Objective:** RaBiT maintains a single shared blueprint, \mathbf{W}_{FP} . The on-the-fly derivation process, $\mathbf{R}_1 := \mathbf{W}_{\text{FP}} - \hat{\mathbf{W}}_1$ followed by the binarization of \mathbf{R}_1 to create $\hat{\mathbf{W}}_2$, explicitly defines the optimization target for the second path. The goal for $\hat{\mathbf{W}}_2$ is no longer to align with the global gradient \mathbf{G} , but to be the best possible low-rank approximation of the current residual \mathbf{R}_1 .

$$\text{Objective for } \hat{\mathbf{W}}_2 : \quad \min \|\mathbf{R}_1 - \hat{\mathbf{W}}_2\|_F^2 \implies \hat{\mathbf{W}}_2 \approx \mathbf{R}_1$$

This structural constraint forces a high **Residual Alignment**. In the context of extreme low-bit quantization, the first approximation $\hat{\mathbf{W}}_1$ often "overshoots" the target \mathbf{W}_{FP} in certain directions. To correct this, the residual $\mathbf{R}_1 = \mathbf{W}_{\text{FP}} - \hat{\mathbf{W}}_1$ will point in the opposite direction of the overshoot. By aligning with \mathbf{R}_1 , $\hat{\mathbf{W}}_2$ naturally becomes **anti-correlated** with $\hat{\mathbf{W}}_1$, implementing an efficient **active cancellation** mechanism rather than degenerating into redundancy.

\square

Proposition 3 (Superior Optimization Dynamics of Coupled vs. Iterative Training). *Iterative training (e.g., freezing one path while training the other) avoids adaptation but at the cost of optimization efficiency. In contrast, RaBiT resolves adaptation while permitting full parameter co-adaptation, resulting in a superior optimization trajectory.*

Proof. Following Proposition 1, the problem of Standard QAT is the simultaneous update of both paths in the same direction. An alternative solution is to update them iteratively, which prevents this simultaneous push and thus avoids adaptation. However, this introduces a new problem of inefficiency.

The optimal direction to reduce the loss \mathcal{L} is the steepest descent direction in the joint parameter space of $(\mathbf{W}_1, \mathbf{W}_2)$, which is $\mathbf{d}^* = (-\mathbf{G}, -\mathbf{G})$. When training iteratively, one path is frozen, so the update is restricted to an axis-aligned direction, e.g., $\mathbf{d}_{\text{iter}} = (\mathbf{0}, -\mathbf{G})$. The cosine similarity between the iterative update and the optimal update direction is:

$$\begin{aligned}\cos(\theta) &= \frac{\langle \mathbf{d}_{\text{iter}}, \mathbf{d}^* \rangle_F}{\|\mathbf{d}_{\text{iter}}\|_F \|\mathbf{d}^*\|_F} = \frac{\langle (\mathbf{0}, -\mathbf{G}), (-\mathbf{G}, -\mathbf{G}) \rangle_F}{\|(\mathbf{0}, -\mathbf{G})\|_F \|(-\mathbf{G}, -\mathbf{G})\|_F} \\ &= \frac{\|\mathbf{G}\|_F^2}{\|\mathbf{G}\|_F \cdot \sqrt{\|\mathbf{G}\|_F^2 + \|\mathbf{G}\|_F^2}} = \frac{1}{\sqrt{2}}\end{aligned}$$

This fixed 45° misalignment forces the optimization to follow an inefficient zig-zag trajectory. While it solves adaptation, it sacrifices optimization efficiency.

RaBiT, through its coupled derivation described in Proposition 2, resolves this trade-off. By updating a single shared weight \mathbf{W}_{FP} with the full gradient \mathbf{G} , it allows both paths to co-adapt simultaneously in a coordinated manner that is not restricted to an inefficient path. Thus, RaBiT resolves adaptation without compromising optimization efficiency, leading to superior dynamics. \square

Corollary 1 (to Proposition 2). Negative Correlation Induction. *RaBiT’s coupled training mechanism, by forcing the second path ($\hat{\mathbf{W}}_2$) to approximate the residual of the first path (\mathbf{R}_1), inherently promotes a negative correlation between their respective outputs ($\mathbf{y}_1, \mathbf{y}_2$).*

Analysis. From Proposition 2, we established that RaBiT trains the second path to approximate the residual of the first:

$$\hat{\mathbf{W}}_2 \approx \mathbf{R}_1 = \mathbf{W}_{\text{FP}} - \hat{\mathbf{W}}_1$$

Let us consider the outputs for a given input \mathbf{x} . The outputs of the full-precision teacher, the first path, and the second path are $\mathbf{y}_t = \mathbf{W}_{\text{FP}}\mathbf{x}$, $\mathbf{y}_1 = \hat{\mathbf{W}}_1\mathbf{x}$, and $\mathbf{y}_2 = \hat{\mathbf{W}}_2\mathbf{x}$, respectively. Based on the weight approximation, the output of the second path is:

$$\mathbf{y}_2 \approx \mathbf{R}_1\mathbf{x} = (\mathbf{W}_{\text{FP}} - \hat{\mathbf{W}}_1)\mathbf{x} = \mathbf{y}_t - \mathbf{y}_1$$

Now, we can analyze the covariance between the outputs \mathbf{y}_1 and \mathbf{y}_2 . Assuming the outputs are centered for simplicity, the covariance is proportional to the expected value of their dot product, $\mathbb{E}[\mathbf{y}_1^\top \mathbf{y}_2]$.

$$\mathbb{E}[\mathbf{y}_1^\top \mathbf{y}_2] \approx \mathbb{E}[\mathbf{y}_1^\top (\mathbf{y}_t - \mathbf{y}_1)] = \mathbb{E}[\mathbf{y}_1^\top \mathbf{y}_t] - \mathbb{E}[\mathbf{y}_1^\top \mathbf{y}_1] = \mathbb{E}[\mathbf{y}_1^\top \mathbf{y}_t] - \mathbb{E}[\|\mathbf{y}_1\|^2]$$

Let us analyze the two terms:

1. $\mathbb{E}[\mathbf{y}_1^\top \mathbf{y}_t]$: The first path $\hat{\mathbf{W}}_1$ is the primary, albeit coarse, approximation of \mathbf{W}_{FP} . Its purpose is to capture the main features of the teacher, so \mathbf{y}_1 and \mathbf{y}_t are expected to be **positively correlated**. However, in the extreme 1-bit regime, the approximation is directionally coarse: a non-negligible portion of \mathbf{y}_1 lies in directions *not* well-aligned with \mathbf{y}_t . This misaligned component limits how large the alignment term $\mathbf{y}_1^\top \mathbf{y}_t$ can become, making the positive correlation typically *not* strong.
2. $\mathbb{E}[\|\mathbf{y}_1\|^2]$: This is the expected squared norm of the first path’s output. Binarization is an aggressive quantization that often leads to an “overshoot” in magnitude. A single binary path must represent a wide range of continuous values, so its effective scaling factor often results in an output magnitude $\|\mathbf{y}_1\|$ that exceeds the projection of \mathbf{y}_1 onto \mathbf{y}_t . Consequently, it is often the case that $\|\mathbf{y}_1\|^2 > \mathbf{y}_1^\top \mathbf{y}_t$, making $\mathbb{E}[\|\mathbf{y}_1\|^2]$ a larger positive term than $\mathbb{E}[\mathbf{y}_1^\top \mathbf{y}_t]$.

Combining these points, the covariance is approximately the difference between a positive term and a larger positive term:

$$\text{Cov}(\mathbf{y}_1, \mathbf{y}_2) \approx \underbrace{\mathbb{E}[\mathbf{y}_1^\top \mathbf{y}_t]}_{\text{Positive Alignment}} - \underbrace{\mathbb{E}[\|\mathbf{y}_1\|^2]}_{\text{Larger Magnitude Term}} < 0$$

Thus, RaBiT’s mechanism of forcing the second path to correct the error of the first path structurally drives the covariance, and therefore the correlation $\text{Corr}(\mathbf{y}_1, \mathbf{y}_2)$, toward negative, consistent with our empirical observations. \square

B. Extended Analysis: Inter-Path Adaptation under KL Divergence

While Section 3 and Corollary 1 motivate RaBiT using the Mean Squared Error (MSE) decomposition, modern LLM training often relies on the Kullback-Leibler (KL) divergence loss. In this section, we rigorously demonstrate that the principle of “inter-path adaptation” and RaBiT’s solution remain valid under the KL divergence objective. We leverage a local quadratic approximation and the findings from (Kim et al., 2021) regarding the decomposition of KL loss.

Proposition 4 (Optimality of Residual Coupling under KL Divergence). *RaBiT’s residual coupling mechanism structurally eliminates the optimization bias inherent in the KL divergence loss by enforcing a negative Hessian-weighted path correlation, a property that Standard QAT fails to satisfy.*

Analysis. We analyze the optimization dynamics at a specific linear layer ℓ where RaBiT is applied. Let $\mathbf{y}_t^\ell = \mathbf{W}_{\text{FP}} \mathbf{x}^\ell$ be the output feature of the teacher model, and \mathbf{y}_s^ℓ be that of the student. Since the operations within the layer are linear, the student’s output is the sum of its binary paths: $\mathbf{y}_s^\ell = \mathbf{h}_1 + \mathbf{h}_2$.

Local Quadratic Approximation. The global KL divergence loss \mathcal{L}_{KL} can be approximated locally around the teacher’s output \mathbf{y}_t^ℓ using a second-order Taylor expansion:

$$\mathcal{L}_{KL}(\mathbf{y}_s^\ell) \approx \mathcal{L}_{KL}(\mathbf{y}_t^\ell) + \nabla \mathcal{L}(\mathbf{y}_t^\ell)^\top \Delta \mathbf{y} + \frac{1}{2} \Delta \mathbf{y}^\top \mathbf{H}^\ell \Delta \mathbf{y} \quad (8)$$

Assuming the teacher is optimal locally ($\nabla \mathcal{L} \approx 0$), the optimization objective reduces to minimizing a **Hessian-weighted MSE**:

$$\mathcal{J}_{local} \approx \frac{1}{2} \|\mathbf{y}_s^\ell - \mathbf{y}_t^\ell\|_{\mathbf{H}^\ell}^2 = \frac{1}{2} (\mathbf{h}_1 + \mathbf{h}_2 - \mathbf{y}_t^\ell)^\top \mathbf{H}^\ell (\mathbf{h}_1 + \mathbf{h}_2 - \mathbf{y}_t^\ell) \quad (9)$$

where \mathbf{H}^ℓ is the Hessian matrix representing the local curvature.

Decomposition with Hessian-weighted Path Correlation. Similar to Equation (1) in the main text, we decompose this local objective. By treating $(\mathbf{h}_1 - \mathbf{y}_t^\ell)$ as the residual error of the first path, we expand the quadratic term:

$$\mathcal{J}_{local} \propto \underbrace{\|\mathbf{h}_1 - \mathbf{y}_t^\ell\|_{\mathbf{H}^\ell}^2}_{\text{Base Error}} + \underbrace{\|\mathbf{h}_2\|_{\mathbf{H}^\ell}^2}_{\text{Path 2 Amp.}} + \underbrace{2(\mathbf{h}_1 - \mathbf{y}_t^\ell)^\top \mathbf{H}^\ell \mathbf{h}_2}_{\text{Interaction Term}} \quad (10)$$

We define the *Hessian-weighted Path Correlation*, denoted as $\text{PathCorr}_{\mathbf{H}}$, based on the generalized cosine similarity in the inner product defined by \mathbf{H}^ℓ :

$$\text{Interaction Term} = 2 \cdot \|\mathbf{h}_1 - \mathbf{y}_t^\ell\|_{\mathbf{H}^\ell} \|\mathbf{h}_2\|_{\mathbf{H}^\ell} \cdot \text{PathCorr}_{\mathbf{H}}(\mathbf{h}_1 - \mathbf{y}_t^\ell, \mathbf{h}_2) \quad (11)$$

This formulation reveals that minimizing the local loss requires maximizing the negative magnitude of $\text{PathCorr}_{\mathbf{H}}$.

Bridging Interaction to Bias Cancellation. To understand the implication of this interaction term in the context of KL divergence, we refer to (Kim et al., 2021), which proved that minimizing \mathcal{L}_{KL} is equivalent to minimizing MSE plus a negative **Bias Term** (δ). This bias term acts as a destabilizing force that pushes the student’s logit sum to diverge from the teacher’s. Crucially, effectively maximizing the negative interaction term (*i.e.*, enforcing error correction) is the key to neutralizing this bias.

- **Failure of Standard QAT:** In Standard QAT, \mathbf{h}_1 and \mathbf{h}_2 are updated independently using the same gradient signal. This leads to \mathbf{h}_2 aligning with \mathbf{y}_t^ℓ rather than the residual $(\mathbf{y}_t^\ell - \mathbf{h}_1)$. Consequently, $\text{PathCorr}_{\mathbf{H}}$ becomes positive (redundancy) or near zero. This failure to exploit the interaction bonus leaves the destabilizing Bias Term (δ) unchecked, causing the optimization drift described in (Kim et al., 2021).
- **Success of RaBiT:** RaBiT enforces $\hat{\mathbf{W}}_2 = \text{sign}(\mathbf{W}_{\text{FP}} - \hat{\mathbf{W}}_1)$, structurally guaranteeing:

$$\mathbf{h}_2 \approx \mathbf{y}_t^\ell - \mathbf{h}_1 = -(\mathbf{h}_1 - \mathbf{y}_t^\ell) \quad (12)$$

This forces the second path vector to be anti-parallel to the first path’s error vector in the feature space. As a result:

1. **Maximized Interaction:** $\text{PathCorr}_{\mathbf{H}}$ approaches its theoretical minimum of -1 (perfect anti-correlation).

2. **Bias Cancellation:** By strictly adhering to the residual $\mathbf{h}_2 \approx \mathbf{y}_t^\ell - \mathbf{h}_1$, the total student output \mathbf{y}_s^ℓ approximates \mathbf{y}_t^ℓ without the scale divergence issues. The Bias Term (δ) is effectively cancelled out locally ($(\sum \mathbf{y}_s^\ell - \sum \mathbf{y}_t^\ell)^2 \approx 0$).

Therefore, RaBiT’s residual coupling is the optimal strategy for minimizing \mathcal{L}_{KL} as it structurally enforces the necessary negative correlation that Standard QAT fails to learn. \square

C. Initialization Analysis: Functionality vs. Approximation

Table 7. Initialization Analysis on Llama2-7B. Trade-off between weight reconstruction error (Avg. MAE/MSE) and model functionality (Initial KL Divergence Loss), for the first `q_proj` layer. I/O Channel Importance Scaling dramatically reduces KL Divergence Loss despite increasing MSE.

Initialization Method	Avg. MAE \downarrow	Avg. MSE \downarrow	KL Loss \downarrow
Greedy SVID	0.359	0.150	17,152
Iterative Residual SVID	0.370	0.122	13,760
+ I/O Ch. Importance Scaling	0.632	0.302	2,672

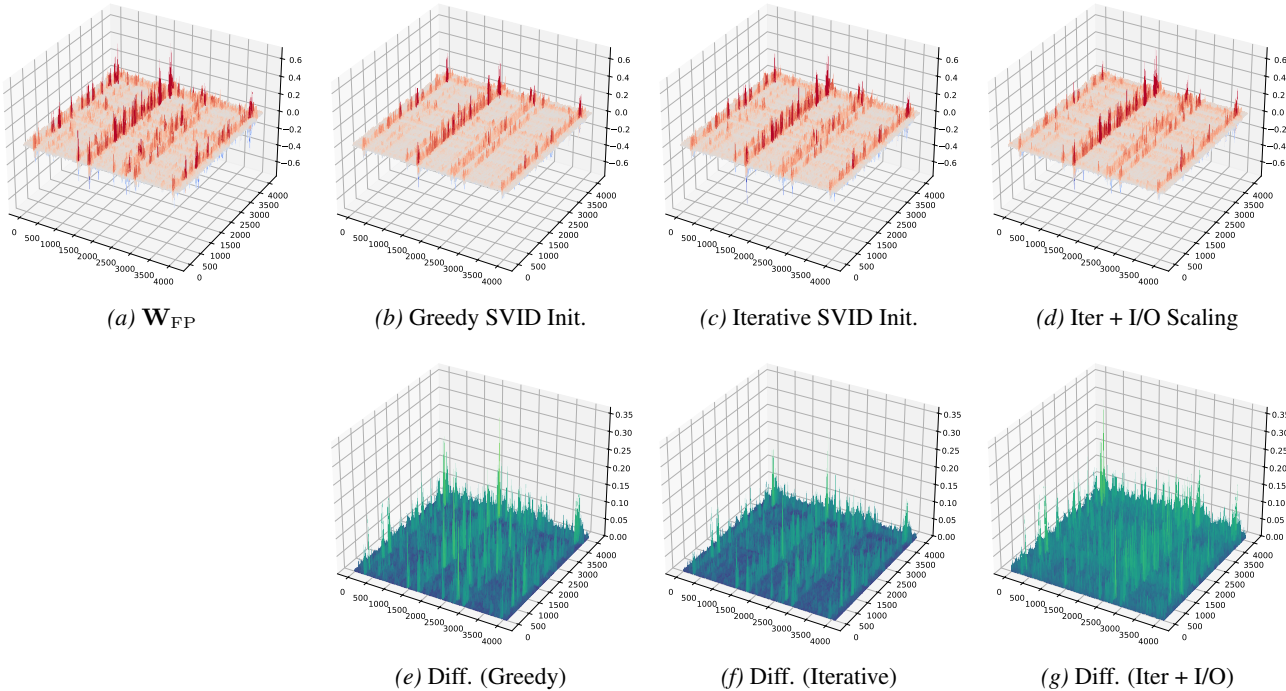


Figure 3. Visual analysis of weight initialization for the first layer’s `q_proj` matrix of the Llama2-7B model. The top row displays the original full-precision weight (\mathbf{W}_{FP}) alongside its initial approximations from three methods: (b) Greedy SVID, (c) Iterative SVID, and (d) Iterative SVID with I/O Channel Importance Scaling. The bottom row shows the corresponding difference matrices ($\mathbf{W}_{FP} - \hat{\mathbf{W}}_{init}$), illustrating the initial error structure. Our function-aware initialization produces a qualitatively different structure compared to the others, which is reflected in its distinct error pattern.

Stable initialization is paramount in the low-bit regime, as the initial quantization error spike can destabilize QAT. On the Llama2-7b model, we evaluate our proposed techniques—Iterative Residual SVID and I/O Channel Importance Scaling (Section 4.3)—by measuring both the weight reconstruction error (Avg. MAE, MSE) and the initial task loss (Knowledge Distillation (KD) loss) before the first training step.

Table 7 details the results for the first `q_proj` layer and reveals a crucial insight. As our baseline, Greedy SVID is a non-iterative decomposition that finalizes each path sequentially without the co-adaptation enabled by our iterative approach. First, regarding **Iterative Refinement**, moving from Greedy SVID to Iterative Residual SVID consistently improves weight reconstruction (e.g., Avg. MSE drops $0.150 \rightarrow 0.122$) and substantially reduces the initial KL divergence loss ($17,152 \rightarrow$

13,760), confirming mitigation of scheduling bias. Second, adding **I/O Channel Importance Scaling** to the iterative process yields a striking result: while reconstruction error increases significantly (Avg. MSE $0.122 \rightarrow 0.302$), the KL divergence loss *plummets* dramatically ($13,760 \rightarrow 2,672$, an 81% reduction).

This confirms that extreme quantization should prioritize preserving *functionality* over merely approximating *weights*. I/O Channel Importance Scaling allocates the limited 2-bit capacity to critical channels based on activation and gradient statistics (Section 4.3), sacrificing the reconstruction of less important weights. This trade-off is visually stark in Figure 3. While Iterative SVID produces a lower-error approximation than Greedy SVID (comparing Figure 3f to Figure 3e), the function-aware I/O Scaling method yields a visibly larger reconstruction error (Figure 3g). Despite this higher weight-level discrepancy, its focus on functional saliency provides a far superior starting point for QAT, as evidenced by the dramatic reduction in initial task loss.

D. Extended Results

Detailed Zero-Shot Reasoning Accuracy. Table 8 and Table 9 provide a detailed breakdown of the zero-shot reasoning accuracy across five common benchmarks, complementing the average scores reported in the main text.

Table 8. Detailed Zero-Shot Reasoning Accuracy on Llama Models (%). Comparison of FP16 against leading 2-bit methods on five common benchmarks.

Models	Method	WinoGrande \uparrow	HellaSwag \uparrow	ARC-e \uparrow	ARC-c \uparrow	PIQA \uparrow	Average \uparrow
Llama2-7B	FullPrecision	67.80	56.71	69.28	39.93	78.29	62.40
	QTIP	64.64	53.09	65.57	35.67	75.90	58.97
	DBF	63.61	52.44	64.73	35.58	75.84	58.44
	RaBiT (Ours)	67.80	53.52	72.43	37.88	75.90	61.51
Llama2-13B	FullPrecision	69.93	59.64	73.19	45.73	78.67	65.43
	QTIP	67.56	57.4	70.8	41.46	77.37	62.92
	DBF	67.09	56.6	69.02	38.74	78.18	61.93
	RaBiT (Ours)	67.56	56.71	69.06	39.76	77.42	62.10
Llama3-8B	FullPrecision	72.93	60.08	80.30	50.17	79.76	67.80
	QTIP	70.24	55.53	75.29	41.64	76.71	63.88
	DBF	68.90	54.49	74.62	39.76	76.44	62.84
	RaBiT (Ours)	69.37	55.13	75.37	42.83	77.96	64.13

Table 9. Detailed Zero-Shot Reasoning Accuracy on Gemma Models (%). Comparison of FP16 against leading 2-bit methods on five common benchmarks.

Models	Method	WinoGrande \uparrow	HellaSwag \uparrow	ARC-e \uparrow	ARC-c \uparrow	PIQA \uparrow	Average \uparrow
Gemma3-1B	FullPrecision	59.59	47.30	72.22	35.32	74.65	57.82
	QTIP	54.62	38.24	63.93	25.85	68.88	50.30
	DBF	58.01	40.37	62.92	28.41	70.18	51.98
	RaBiT (Ours)	56.59	42.94	64.52	29.44	72.42	53.18
Gemma3-4B	FullPrecision	69.22	56.77	81.52	51.45	79.05	67.60
	QTIP	66.85	52.25	77.53	44.62	76.12	63.47
	DBF	63.69	50.15	74.74	40.87	75.08	60.91
	RaBiT (Ours)	65.19	52.57	75.04	41.38	76.88	62.21
Gemma3-12B	FullPrecision	75.45	61.98	87.08	61.60	81.12	73.45
	QTIP	72.69	57.99	84.09	54.95	78.73	69.69
	DBF	72.14	57.20	82.49	52.05	77.97	68.37
	RaBiT (Ours)	72.30	58.45	82.41	52.13	78.95	68.85

E. Inference Performance Analysis

E.1. Kernel Design

Our CUDA kernels implement binary GEMV operations tailored to the memory-bound regime typical of the decoding phase in LLM inference. The design centers on bit-packing to reduce global memory traffic, with a latency-tolerant and matmul-free compute pipeline that leverages register-level staging.

Weight Packing. To reduce memory traffic, each group of 32 columns is mapped to a `uint32_t`, with $+1 \mapsto 0$ and $-1 \mapsto 1$. We then group the 32-bit words into `uint2` or `PackedBits3` (3 `uint32_t` weights with padding), for 2-bit (2 binary weights) and 3-bit (3 binary weights) models, respectively. Rows are interleaved into warp-sized groups, ensuring that a warp issues full coalesced memory transactions when loading weights. Our efficient packing reduces the raw footprint of weights by a factor of $32\times$, compared to full-precision weights.

Compute Pipeline. Each warp is assigned a set of output rows to avoid inter-warp synchronization. Input activations (x) and column scales (g) are read as vectorized `uint4` chunks. Binary signs are applied via lane-local bit shifts and XOR masks, instead of matrix multiplication. The kernel uses simple yet effective pipelining: while one tile of data is consumed, the subsequent tile is prefetched into registers. Accumulation proceeds using `half2` fused multiply-add intrinsics (`__hfma2`), which increase arithmetic throughput without resorting to shared memory. Finally, reductions across threads in a warp are performed with shuffle operations, and output scale factors (h) are applied in `fp16` precision. Notably, our architecture enables per-path parallelizable computation - instead of an n -bit weight, we parallelize with n 1-bit operations.

Efficient weight packing and pipelining reduce global memory access and raise the utilization of execution units on the GPU. The kernel therefore shifts the limiting factor from raw memory bandwidth toward register throughput, yielding measurable efficiency gains during the decoding stage of LLM inference, showing remarkable performance.

E.2. More Comparisons

To provide a more detailed analysis of the end-to-end inference speed, we benchmarked RaBiT against several key baselines: the full-precision (FP16) model, QTIP as the state-of-the-art Vector Quantization (VQ) method, and DBF, which features a similar stacked binary architecture. For QTIP, we utilized the publicly available CUDA kernels from the official implementation³. For DBF, which also uses a stacked binary design but executes its two paths sequentially, we developed

³<https://github.com/Cornell-RelaxML/qtip>

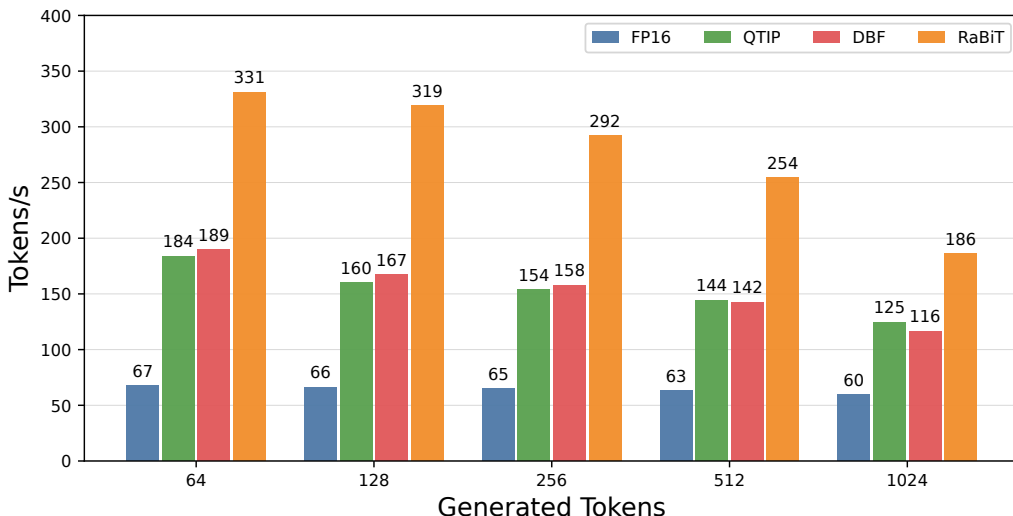


Figure 4. End-to-end decoding throughput (tokens/second) for Llama2-7B on an NVIDIA RTX 4090 across various generated token lengths. RaBiT’s parallel architecture consistently delivers superior performance over other 2-bit methods.

an optimized CUDA kernel that runs approximately 21% faster than their public Triton-based implementation to ensure a fair and robust comparison. All evaluations were conducted on an NVIDIA RTX 4090 with `torch.compile` using the Llama2-7B model.

The results, depicted in Figure 4, were benchmarked across a range of generated token lengths (64, 128, 256, 512, and 1024) for a comprehensive analysis. As expected, all 2-bit methods significantly outperform the FP16 baseline due to the $8\times$ reduction in memory bandwidth requirements. More importantly, **RaBiT demonstrates a substantial performance advantage, achieving nearly twice the decoding throughput** of the other 2-bit quantization methods. This speed-up stems directly from the efficiency of our parallel, matmul-free architecture. Unlike DBF, which is bottlenecked by its sequential computation of two binary paths, RaBiT’s fully parallel design allows it to maximally leverage the benefits of its efficient binary cores. While the absolute tokens/second rate naturally decreases with longer generation sequences, the relative performance gap between the methods remains consistent, confirming the robustness of RaBiT’s architectural advantage.

F. Hyperparameters

F.1. Training Details

We detail the hyperparameters used for our Quantization-aware training (QAT) experiments in Table 10. All models were trained for 6 epochs using the Muon optimizer (Jordan et al., 2024) with a cosine learning rate decay schedule. The models were initialized using our proposed function-aware strategy, with a fixed SVID iteration count of $T_{\max} = 20$. Key hyperparameters, such as the learning rate and the I/O Channel Importance Scaling intensities ($\alpha_{in}, \alpha_{out}$), were fine-tuned for each specific model to achieve the best performance. All experiments were conducted on a single node equipped with four NVIDIA H100 GPUs.

Table 10. Hyperparameter Configuration. We detail the training settings including learning rates, intensities ($\alpha_{in}, \alpha_{out}$), and batch information for the Llama and Gemma model families.

Bit	Target	Training Setup		Llama2		Llama3		Gemma3		
		7B	13B	8B	1B	4B	12B			
2	Intensities ($\alpha_{in}, \alpha_{out}$)	(0.8, 0.65)	(0.95, 0.45)	(0.85, 0.7)	(0.85, 0.7)	(0.95, 0.7)	(0.75, 0.6)			
	Iteration (T_{\max})	20	20	20	20	20	20			
	Learning Rate	12e-6	1e-5	1e-5	1e-5	1e-5	5e-6			
	Epoch	6	6	6	6	6	6			
	# GPUs	1 \times 4	1 \times 4	1 \times 4	1 \times 4	1 \times 4	1 \times 4			
	# Training Hours	39	56	38	8	23	67			
3	Intensities ($\alpha_{in}, \alpha_{out}$)	(0.8, 0.65)	(0.95, 0.45)	(0.85, 0.7)	-	-	-			
	Iteration (T_{\max})	20	20	20	-	-	-			
	Learning Rate	1e-5	1e-5	1e-5	-	-	-			
	Epoch	6	6	6	-	-	-			
	# GPUs	1 \times 4	1 \times 4	1 \times 4	-	-	-			
	# Training Hours	46	88	44	-	-	-			

F.2. Grid Search for I/O Channel Importance Scaling Intensities

To determine the optimal intensity hyperparameters for our I/O Channel Importance Scaling (Section 4.3), we performed a comprehensive grid search. The objective was to identify the values of α_{in} and α_{out} that minimized the initial Knowledge Distillation (KD) loss post-initialization. This process utilized a calibration dataset of 128 samples randomly selected from the training data to measure the loss.

The example results of this search on the Llama2-7B model are detailed in Table 11. We observed a clear optimum, with the minimum initial KL divergence loss of 2,672 achieved at the configuration of $\alpha_{in} = 0.80$ and $\alpha_{out} = 0.65$. This finding underscores the importance of a balanced preconditioning strategy that considers both input activation statistics and output gradient magnitudes. **We repeated this grid search process for all other models to find their optimal alpha values.**

Table 11. Grid search results for I/O Channel Importance Scaling Intensities (α_{in} , α_{out}) on Llama2-7B. The metric is the Initial KL Divergence Loss (Lower is better). The optimal configuration is highlighted in bold.

α_{out}	α_{in}			
	0.75	0.80	0.85	0.90
0.55	3,100	2,932	2,984	3,108
0.60	2,932	2,938	2,971	3,143
0.65	3,167	2,672	2,697	3,063
0.70	3,083	2,821	2,983	3,462

F.3. SVID Iteration Convergence Analysis

The Iterative Residual SVID initialization (Section 4.3) aims to mitigate the scheduling bias inherent in standard greedy initialization. We analyzed the required number of iterations (T_{max}) for convergence on the Llama2-7B model. We measured the Initial KL divergence loss as the iterations progressed from 1 (equivalent to Greedy SVID) up to 35.

The results, shown in Figure 5, indicate that the initialization quality improves rapidly in the initial phase. The loss stabilizes significantly around 15 iterations, and the optimum is reached at 20 iterations. Beyond this point, further iterations do not provide additional benefits. Based on this analysis, we selected $T_{\text{max}} = 20$ as the default setting for RaBiT initialization, providing an optimal balance between initialization quality and computational cost.

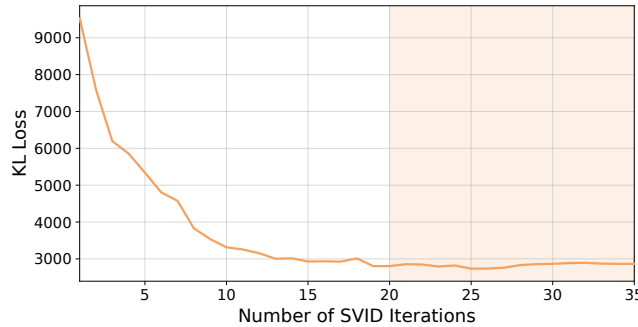


Figure 5. Convergence analysis of Iterative Residual SVID on Llama2-7B. The metric is the Initial KL Divergence Loss (Lower is better). Convergence stabilizes around 20 iterations.

G. Extended Analysis of Inter-Path Adaptation

To provide a more granular view of the training dynamics, we conduct a layer-wise analysis of the Mean Squared Error (MSE) decomposition for the Llama2-7B model, visualized in Figure 6. This analysis offers two key insights into RaBiT’s structural advantages over Standard QAT.

First, the results empirically confirm our central hypothesis across the network’s depth. For most layers, RaBiT consistently generates a substantial negative covariance (the red-dashed component), which acts as a significant loss-reducing bonus, thereby lowering the total MSE. In contrast, Standard QAT fails to establish this effective error-cancellation, exhibiting a much smaller covariance term that provides negligible benefit. This provides strong visual evidence that RaBiT’s coupled training successfully enforces the intended error-correction hierarchy, while Standard QAT suffers from the performance degradation of inter-path adaptation.

Second, and more strikingly, the analysis reveals RaBiT’s ability to overcome a critical optimization challenge in extreme quantization: layer sensitivity. The Standard QAT baseline exhibits an exceptionally high MSE in the initial layers, a phenomenon consistent with the known sensitivity of early network layers to input distributions and quantization errors, as also observed in other LLMs by (Zhang et al., 2025; 2024). RaBiT, however, dramatically suppresses this MSE peak. This suggests its benefits extend beyond merely enforcing anti-correlation. The fact that RaBiT tames this instability indicates that our method may resolve a more fundamental bottleneck in MSE-based QAT that has historically hindered extreme quantization in conventional architectures. While we designed RaBiT to foster negative correlation, its success in stabilizing

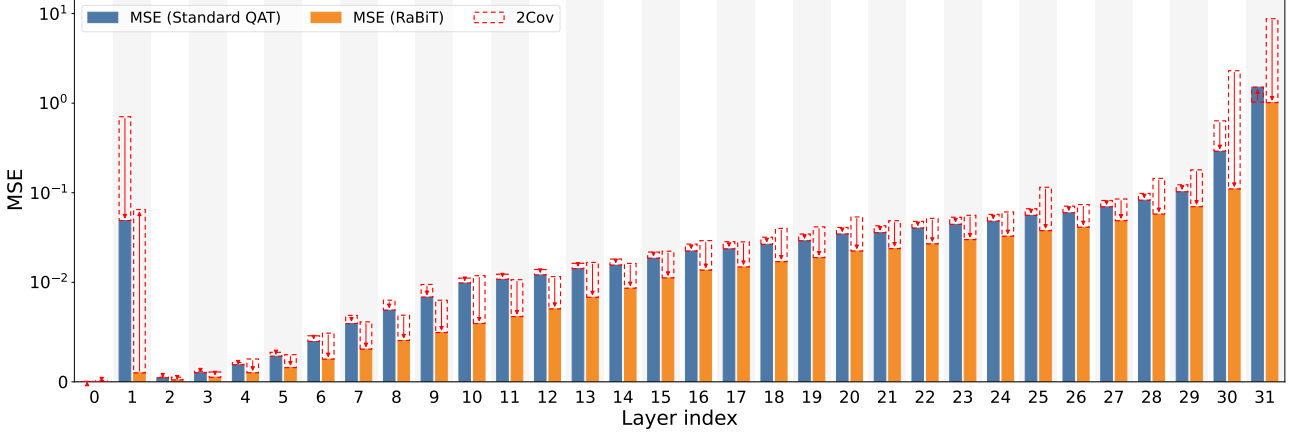


Figure 6. Layer-wise MSE Decomposition in Llama2-7B’s `down_proj` layers. The bars compare the total Mean Squared Error (MSE) for Standard QAT (blue) and RaBiT (orange). The top of each bar represents the base error term (C'), while the red-dashed component visualizes twice the covariance ($2 \times \text{Cov}$). RaBiT consistently generates a large negative covariance, which actively reduces the total MSE, demonstrating effective error cancellation. Notably, RaBiT also suppresses the extremely high MSE peak observed in the early layers of the Standard QAT baseline, indicating its robustness against layer sensitivity.

these sensitive layers points to a deeper robustness. A full investigation into how residual coupling imparts this stability is a compelling direction for future research.

H. Generated Samples

Sample 1: Newton

Prompt: Newton discovered the law of universal gravitation. Universal gravitation is

Generated Output

Newton discovered the law of universal gravitation. Universal gravitation is the force of gravity which draws objects towards the earth and other massive bodies. Gravity is the universal attraction between two objects and is proportional to the product of the masses of the two objects and inversely proportional to the square of the distance between them. Newton explained the force of gravity as being caused by the presence of matter in the universe. He stated that all matter attracted all other matter and that the tendency to move towards a massive body was proportional to the product of the masses of the objects. Newton developed the law of universal gravitation so that the attraction between two bodies could be calculated.

Sample 2: Adam Smith

Prompt: Adam Smith wrote The Wealth of Nations. The Wealth of Nations is

Generated Output

Adam Smith wrote The Wealth of Nations. The Wealth of Nations is the first book to outline the modern principles of capitalism and to make the case for it. Smith's work is widely considered to be the first comprehensive system of political economy and one of the most important works of political philosophy. The Wealth of Nations is the foundation of modern capitalism. The Wealth of Nations is a book by Adam Smith, first published in 1776, which describes the nature of economic systems. Adam Smith is regarded as the father of modern economics. The Wealth of Nations is widely considered to be the first comprehensive system of political economy and one of the most important works of political philosophy. It is also one of the most influential books on economics. Adam Smith is regarded as the father of modern economics.

Sample 3: DNA double helix

Prompt: Watson and Crick discovered the DNA double helix. The DNA double helix is

Generated Output

Watson and Crick discovered the DNA double helix. The DNA double helix is a structure found in the nucleus of every living cell. The double helix is the most fundamental structure in DNA. The structure is made of two single strands of DNA. The double helix was discovered in 1953 by James Watson and Francis Crick. In 1953, James Watson and Francis Crick discovered the double helix structure of DNA. The double helix structure is the most fundamental structure in DNA. The double helix structure is made of two single strands of DNA. The double helix is found in the nucleus of every living cell.

I. Algorithms

Algorithm 1 RaBiT Initialization: Calibrated Iterative Residual SVID

```

1: Require: Pretrained weight  $\mathbf{W}_{\text{FP}}$ , Number of paths  $k$ , Max iterations  $T_{\max}$ 
2: Require: Calibration stats  $\mathbf{s}_{\text{in}}, \mathbf{s}_{\text{out}}$  and intensities  $\alpha_{\text{in}}, \alpha_{\text{out}}$ 
3: Output: Initialized scales  $\{(\mathbf{g}_i, \mathbf{h}_i)\}_{i=1}^k$ 

4: // Step 1: I/O Channel Importance-Calibrated Preconditioning
5: Normalize:  $\mathbf{s}_{\text{in}} \leftarrow \mathbf{s}_{\text{in}} / \max(\mathbf{s}_{\text{in}})$ ,  $\mathbf{s}_{\text{out}} \leftarrow \mathbf{s}_{\text{out}} / \max(\mathbf{s}_{\text{out}})$ 
6: Precondition:  $\mathbf{W}' \leftarrow \mathbf{s}_{\text{out}}^{\alpha_{\text{out}}} \odot \mathbf{W}_{\text{FP}} \odot \mathbf{s}_{\text{in}}^{\alpha_{\text{in}}}$ 

7: // Step 2: Iterative Residual SVID
8: Initialize  $\hat{\mathbf{W}}_i^{(0)} \leftarrow \mathbf{0}$  for  $i = 1, \dots, k$ 
9: for  $t = 1$  to  $T_{\max}$  do
10:   for  $i = 1$  to  $k$  do
11:     // Calculate target residual (Gauss-Seidel style update)
12:      $\mathbf{R}_i^{(t)} \leftarrow \mathbf{W}' - \left( \sum_{j < i} \hat{\mathbf{W}}_j^{(t)} + \sum_{j > i} \hat{\mathbf{W}}_j^{(t-1)} \right)$ 
13:     // Apply SVID to find the best rank-1 approximation
14:      $(\mathbf{B}_i^{(t)}, \mathbf{g}_i^{(t)}, \mathbf{h}_i^{(t)}) \leftarrow \text{SVID}(\mathbf{R}_i^{(t)})$ 
15:      $\hat{\mathbf{W}}_i^{(t)} \leftarrow \mathbf{g}_i^{(t)} \odot \mathbf{B}_i^{(t)} \odot \mathbf{h}_i^{(t)}$ 
16:   end for
17: end for

18: // Step 3: Map scales back to the original weight domain
19: for  $i = 1$  to  $k$  do
20:    $\mathbf{g}_i \leftarrow \mathbf{s}_{\text{out}}^{-\alpha_{\text{out}}} \odot \mathbf{g}_i^{(T_{\max})}$ 
21:    $\mathbf{h}_i \leftarrow \mathbf{s}_{\text{in}}^{-\alpha_{\text{in}}} \odot \mathbf{h}_i^{(T_{\max})}$ 
22: end for

```

Algorithm 2 RaBiT: Residual-Aware Binarization Training (One Step)

```

1: Parameters: Shared full-precision weight  $\mathbf{W}_{\text{FP}}$ ; Scales  $\{(\mathbf{g}_i, \mathbf{h}_i)\}_{i=1}^k$ .
2: Input: Minibatch Input  $\mathbf{X}$ , Targets  $\mathbf{T}$ .

3: // 1. Forward Pass: On-the-fly Residual Coupling
4:  $\mathbf{R}_0 \leftarrow \mathbf{W}_{\text{FP}}$ . // Initialize residual with the shared weight
5:  $\hat{\mathbf{W}}^{(k)} \leftarrow \mathbf{0}$ . // Effective weight for the entire layer
6: for  $i = 1$  to  $k$  do
7:   // Sequentially derive the  $i$ -th binary path
8:    $\mathbf{B}_i \leftarrow \text{sign}(\mathbf{R}_{i-1})$ .
9:    $\hat{\mathbf{W}}_i \leftarrow \mathbf{g}_i \odot \mathbf{B}_i \odot \mathbf{h}_i$ .
10:   $\hat{\mathbf{W}}^{(k)} \leftarrow \hat{\mathbf{W}}^{(k)} + \hat{\mathbf{W}}_i$ .
11:  // Update residual for the next path
12:   $\mathbf{R}_i \leftarrow \mathbf{R}_{i-1} - \hat{\mathbf{W}}_i$ .
13: end for
14:  $\mathbf{Y} \leftarrow \hat{\mathbf{W}}^{(k)} \mathbf{X}$ . // Compute layer output
15: Calculate Loss  $\mathcal{L}(\mathbf{Y}, \mathbf{T})$ .

16: // 2. Backward Pass
17:  $\Delta \leftarrow \partial \mathcal{L} / \partial \mathbf{Y}$ . (Output gradient)
18: // Surrogate gradient for the shared weight  $\mathbf{W}_{\text{FP}}$ 
19:  $\nabla_{\mathbf{W}_{\text{FP}}} \leftarrow \Delta \mathbf{X}^\top$ .
20: // Gradients for scales (treating  $\mathbf{B}_i$  as constant)
21: for  $i = 1$  to  $k$  do
22:   Compute  $\nabla_{\mathbf{g}_i}$  and  $\nabla_{\mathbf{h}_i}$  using  $\Delta, \mathbf{B}_i, \mathbf{X}$ , and other scales.
23: end for

24: // 3. Parameter Update
25: Update  $\{\mathbf{W}_{\text{FP}}, (\mathbf{g}_i, \mathbf{h}_i)_{i=1}^k\}$  using an optimizer with the computed gradients.

```

J. Core Kernel Code

```

1  #include <ATen/cuda/CUDAContext.h>
2  #include <c10/cuda/CUDAException.h>
3  #include <c10/cuda/CUDAGuard.h>
4  #include <c10/macros/Macros.h>
5  #include <cuda_fp16.h>
6  #include <cuda_runtime.h>
7  #include <torch/extension.h>
8
9  #include <sstream>
10 #include <string>
11 #include <type_traits>
12
13 // =====
14 // === Macros & Constants ===
15 // =====
16
17 #define CHECK_CUDA(x) TORCH_CHECK(x.is_cuda(), #x " must be a CUDA tensor")
18 #define CHECK_CONTIGUOUS(x) TORCH_CHECK(x.is_contiguous(), #x " must be contiguous")
19 #define CHECK_F16(x) TORCH_CHECK(x.scalar_type() == torch::kFloat16, #x " must be float16 tensor")
20 #define CHECK_INT32(x) TORCH_CHECK(x.scalar_type() == torch::kInt32, #x " tensor dtype must be int32")
21
22 #define CHECK_CUDA_CONT_F16(x) \
23     do { \
24         CHECK_CUDA(x); \
25         CHECK_CONTIGUOUS(x); \
26         CHECK_F16(x); \
27     } while (0)
28
29 #define CHECK_CUDA_CONT_INT32(x) \
30     do { \
31         CHECK_CUDA(x); \
32         CHECK_CONTIGUOUS(x); \
33         CHECK_INT32(x); \
34     } while (0)
35
36 constexpr int WARP_SIZE = 32;
37 constexpr uint32_t SIGN_MASK_U32 = 0x80008000u;
38 constexpr unsigned FULL_MASK = 0xffffffff;
39
40 // =====
41 // === Device Helper Functions ===
42 // =====
43
44 static __device__ __forceinline__ uint32_t half2_to_uint32(const half2& h) {
45     return reinterpret_cast<const uint32_t&>(h);
46 }
47
48 static __device__ __forceinline__ half2 uint32_to_half2(uint32_t v) {
49     return reinterpret_cast<const half2&>(v);
50 }
51
52 // Sign-flipping utility.
53 // Logic: bits determine if we flip the sign of the float16 values packed in uint4.
54 __device__ __forceinline__ uint4 apply_sign(uint4 x4, uint32_t bits, int shift_base) {
55     uint32_t shifted = bits << shift_base;
56     x4.x ^= shifted & SIGN_MASK_U32;
57     x4.y ^= (shifted << 1) & SIGN_MASK_U32;
58     x4.z ^= (shifted << 2) & SIGN_MASK_U32;
59     x4.w ^= (shifted << 3) & SIGN_MASK_U32;
60     return x4;
61 }
62
63 // =====
64 // === Kernel Implementation ===
65 // =====
66
67 template <unsigned NUM_THREAD, unsigned NUM_ROW_PER_WARP = 2, unsigned NUM_ACC = 4, unsigned
68     NUM_PIPELINE_STAGE = 2>
69     __forceinline__ __device__ void rabit_2bit_half_impl(
70         const half* __restrict__ x,
71         const half* __restrict__ scale_g_0,
72         const uint32_t* __restrict__ Wbits,
73         const half* __restrict__ scale_h_0,
74         const half* __restrict__ scale_g_1,
75         const half* __restrict__ scale_h_1,
76         half* __restrict__ y,
77         int N, int M) {
78
79     // Constraints

```

```

79     static_assert(NUM_ROW_PER_WARP == 2, "Only 2 rows per warp supported currently");
80     static_assert(NUM_THREAD % WARP_SIZE == 0, "Threads must be multiple of warp size");
81
82     constexpr unsigned NUM_WARP = NUM_THREAD / WARP_SIZE;
83     constexpr unsigned NUM_ROW_PER_BLOCK = NUM_ROW_PER_WARP * NUM_WARP;
84
85     // Identifiers
86     const int tid = threadIdx.x % WARP_SIZE;
87     const int wid = threadIdx.x / WARP_SIZE;
88
89     // Vectorized pointers (loading 128-bit chunks / 8 halves at a time)
90     const uint4* x8s = reinterpret_cast<const uint4*>(x);
91     const uint4* sg8s_0 = reinterpret_cast<const uint4*>(scale_g_0);
92     const uint4* sg8s_1 = reinterpret_cast<const uint4*>(scale_g_1);
93
94     // Data Structures for Pipelining
95     struct RowAccum {
96         half2 plane[2][NUM_ACC];
97     };
98     struct ColumnScalePair {
99         uint4 g0;
100        uint4 g1;
101    };
102    struct StageTile {
103        uint4 x;
104        ColumnScalePair scale;
105        uint32_t bits;
106    };
107    struct RowContext {
108        int index;
109        RowAccum acc;
110    };
111
112    RowContext rows[NUM_ROW_PER_WARP] = {};
113    StageTile pipe[NUM_PIPELINE_STAGE];
114
115    // Setup Row Indices
116    const int block_row_base = blockIdx.x * NUM_ROW_PER_BLOCK;
117    #pragma unroll
118    for (unsigned irow = 0; irow < NUM_ROW_PER_WARP; ++irow) {
119        rows[irow].index = block_row_base + static_cast<int>(wid) * NUM_ROW_PER_WARP + static_cast<int>(irow);
120    }
121
122    // Weight Bit Indexing
123    // N8 = Number of 8-half chunks (128-bit words)
124    const int N8 = N >> 3;
125    const int wordsN = N8;
126    const int tile_stride = wordsN;
127    const int tile_idx = blockIdx.x * NUM_WARP + wid;
128    const uint32_t* tile_ptr = Wbits + tile_idx * tile_stride;
129
130    // --- Helper Lambdas ---
131
132    auto load_to_reg = [&] (int ireg, int idx8) {
133        StageTile& stage = pipe[ireg];
134        stage.x = x8s[idx8];
135        stage.scale.g0 = sg8s_0[idx8];
136        stage.scale.g1 = sg8s_1[idx8];
137        stage.bits = *(tile_ptr + idx8);
138    };
139
140    // Accumulator indices for circular buffer usage or simple unrolling
141    const int MASK = NUM_ACC - 1;
142    auto fma = [&] (const uint4& scale, const uint4& x, half2 acc[NUM_ACC]) {
143        acc[0] = __hfma2(uint32_to_half2(scale.x), uint32_to_half2(x.x), acc[0]);
144        acc[1 & MASK] = __hfma2(uint32_to_half2(scale.y), uint32_to_half2(x.y), acc[1 & MASK]);
145        acc[2 & MASK] = __hfma2(uint32_to_half2(scale.z), uint32_to_half2(x.z), acc[2 & MASK]);
146        acc[3 & MASK] = __hfma2(uint32_to_half2(scale.w), uint32_to_half2(x.w), acc[3 & MASK]);
147    };
148
149    auto calc_main = [&] (int ireg) {
150        StageTile& stage = pipe[ireg];
151        #pragma unroll
152        for (unsigned irow = 0; irow < NUM_ROW_PER_WARP; ++irow) {
153            RowAccum& acc = rows[irow].acc;
154            // Apply sign logic based on bits (0 or 1 selects path)
155            // 0 + 8*irow and 4 + 8*irow are specific bit shifts for the packed format
156            fma(stage.scale.g0, apply_sign(stage.x, stage.bits, 0 + 8 * irow), acc.plane[0]);
157            fma(stage.scale.g1, apply_sign(stage.x, stage.bits, 4 + 8 * irow), acc.plane[1]);
158        }
159    };

```

```

160
161     // --- Main Loop (Pipelined) ---
162
163     int idx_load = tid;
164     int idx_calc = tid;
165
166     // Prologue: Fill pipeline
167     #pragma unroll
168     for (int istg = 0; istg < NUM_PIPELINE_STAGE; ++istg) {
169         if (idx_load < N8) {
170             load_to_reg(istg, idx_load);
171         }
172         idx_load += WARP_SIZE;
173     }
174
175     // Steady state
176     const int bound_mainloop = N8 - (NUM_PIPELINE_STAGE * WARP_SIZE);
177     while (idx_calc < bound_mainloop) {
178         #pragma unroll
179         for (int istg = 0; istg < NUM_PIPELINE_STAGE; ++istg) {
180             calc_main(istg);
181         }
182         #pragma unroll
183         for (int istg = 0; istg < NUM_PIPELINE_STAGE; ++istg) {
184             if (idx_load < N8) {
185                 load_to_reg(istg, idx_load);
186             }
187             idx_load += WARP_SIZE;
188             idx_calc += WARP_SIZE;
189         }
190     }
191
192     // Epilogue: Drain pipeline
193     #pragma unroll
194     for (int istg = 0; istg < NUM_PIPELINE_STAGE; ++istg) {
195         if (idx_calc < N8) {
196             calc_main(istg);
197             idx_calc += WARP_SIZE;
198         }
199         if (idx_load < N8) {
200             load_to_reg(istg, idx_load);
201             idx_load += WARP_SIZE;
202         }
203     }
204
205     // --- Reduction & Output ---
206
207     auto warp_sum_half = [](half v) {
208         half2 h2 = __halves2half2(v, __float2half(0.0f));
209         #pragma unroll
210         for (int off = WARP_SIZE >> 1; off > 0; off >>= 1) {
211             half2 other = __shfl_xor_sync(FULL_MASK, h2, off);
212             h2 = __hadd2(h2, other);
213         }
214         return __low2half(h2);
215     };
216
217     #pragma unroll
218     for (unsigned irow = 0; irow < NUM_ROW_PER_WARP; ++irow) {
219         RowContext& row = rows[irow];
220         const int out_i = row.index;
221         RowAccum& acc = row.acc;
222
223         half2 lane_acc_0 = __float2half2_rn(0.0f);
224         half2 lane_acc_1 = __float2half2_rn(0.0f);
225
226         #pragma unroll
227         for (unsigned iacc = 0; iacc < NUM_ACC; ++iacc) {
228             lane_acc_0 = __hadd2(lane_acc_0, acc.plane[0][iacc]);
229             lane_acc_1 = __hadd2(lane_acc_1, acc.plane[1][iacc]);
230         }
231
232         // Horizontal sum within registers (half2 -> half)
233         half sum0_h = __hadd(__low2half(lane_acc_0), __high2half(lane_acc_0));
234         half sum1_h = __hadd(__low2half(lane_acc_1), __high2half(lane_acc_1));
235
236         // Apply final scaling factors (h0, h1) and combine paths
237         half lane_total_h = __hfma(sum0_h, scale_h_0[out_i], __hmul(sum1_h, scale_h_1[out_i]));
238
239         // Cross-lane reduction
240         half warp_sum_h = warp_sum_half(lane_total_h);

```

```

241
242     if (tid == 0) {
243         y[out_i] = warp_sum_h;
244     }
245 }
246 }
247
248 template <unsigned NUM_THREAD, unsigned NUM_ROW_PER_WARP = 2, unsigned NUM_ACC = 4, unsigned
249     NUM_PIPELINE_STAGE = 2>
250     __launch_bounds__(NUM_THREAD) __global__ void rabbit_2bit_half_dyn_kernel(
251     const half* __restrict__ x,
252     const half* __restrict__ scale_g_0,
253     const uint32_t* __restrict__ Wbits,
254     const half* __restrict__ scale_h_0,
255     const half* __restrict__ scale_g_1,
256     const half* __restrict__ scale_h_1,
257     half* __restrict__ y,
258     int N, int M) {
259
260     const int s = blockIdx.y;
261     // Offset for batch size (sequence length)
262     const half* x_ptr_for_this_seq = x + s * N;
263     half* y_ptr_for_this_seq = y + s * M;
264
265     rabbit_2bit_half_impl<NUM_THREAD, NUM_ROW_PER_WARP, NUM_ACC, NUM_PIPELINE_STAGE>(
266         x_ptr_for_this_seq, scale_g_0, Wbits, scale_h_0, scale_g_1, scale_h_1, y_ptr_for_this_seq, N, M);
267 }
268
269 // =====
270 // === Template Dispatcher ===
271 // =====
272
273 // Helper to sweep through a compile-time list of values.
274 template <typename T, T... values>
275 struct parameter_sweep {
276     template <typename F, typename U>
277     void operator()(const char* name, U runtime_value, F& func) const {
278         bool found = false;
279         // Fold expression to iterate over template values
280         (
281             [&] () {
282                 if (!found && runtime_value == values) {
283                     std::forward<decltype(func)>(func)(std::integral_constant<T, values>{});
284                     found = true;
285                 }
286             }(),
287             ...
288         );
289         if (!found) {
290             std::stringstream ss;
291             bool is_first = true;
292             ((is_first ? ss : (ss << ", ")) << values, is_first = false), ...);
293             TORCH_CHECK(false, name, " should be one of [", ss.str(), "], but ", runtime_value, " was given");
294         }
295     };
296
297 // =====
298 // === C++ Interface ===
299 // =====
300
301 torch::Tensor rabbit_2bit_half_dyn_forward(
302     torch::Tensor x,
303     torch::Tensor scale_g_0, torch::Tensor Wbits, torch::Tensor scale_h_0,
304     torch::Tensor scale_g_1, torch::Tensor scale_h_1,
305     int64_t num_thread, int64_t num_row_per_warp, int64_t num_acc, int64_t num_pipeline_stage) {
306
307     CHECK_CUDA_CONT_F16(x);
308     CHECK_CUDA_CONT_F16(scale_g_0);
309     CHECK_CUDA_CONT_INT32(Wbits);
310     CHECK_CUDA_CONT_F16(scale_h_0);
311     CHECK_CUDA_CONT_F16(scale_g_1);
312     CHECK_CUDA_CONT_F16(scale_h_1);
313
314     TORCH_CHECK(x.dim() == 1 || x.dim() == 2, "Dynamic Half: x must be 1D or 2D");
315
316     const int seqlen = x.dim() == 1 ? 1 : static_cast<int>(x.size(0));
317     const int N = static_cast<int>(x.size(-1));
318     const int M = static_cast<int>(scale_h_0.size(0));
319
320     // Validations

```

```

321 TORCH_CHECK(scale_g_0.size(0) == N, "Dynamic Half: scale_g_0 size mismatch");
322 TORCH_CHECK(scale_h_0.size(0) == M, "Dynamic Half: scale_h_0 size mismatch");
323 TORCH_CHECK(scale_g_1.size(0) == N, "Dynamic Half: scale_g_1 size mismatch");
324 TORCH_CHECK(scale_h_1.size(0) == M, "Dynamic Half: scale_h_1 size mismatch");
325 TORCH_CHECK((N % 32 == 0), "Dynamic Half: N must be multiple of 32");
326 TORCH_CHECK(num_row_per_warp > 0, "Dynamic Half: num_row_per_warp must be positive");
327
328 const int rows_per_warp = static_cast<int>(num_row_per_warp);
329 TORCH_CHECK(M % rows_per_warp == 0, "Dynamic Half: rows_per_warp must divide output size");
330 TORCH_CHECK(Wbits.dim() == 2 && Wbits.size(0) == M / rows_per_warp && Wbits.size(1) == N / 8,
331 "Dynamic Half: Wbits shape mismatch");
332
333 auto y = torch::empty({long longseqlen, long longM}, x.options());
334
335 at::cuda::CUDAGuard guard(x.device());
336 auto stream = at::cuda::getCurrentCUDAStream();
337
338 // Template Sweepers
339 parameter_sweep<unsigned, 32u, 64u, 128u, 256u, 512u, 1024u> sweep_num_thread;
340 parameter_sweep<unsigned, 2> sweep_row_per_warp;
341 parameter_sweep<unsigned, 1, 2, 4> sweep_num_acc;
342 parameter_sweep<unsigned, 1, 2, 3, 4> sweep_pipeline_stage;
343
344 // Dispatcher
345 auto kernel_func = [=] (auto num_thread_c, auto num_row_per_warp_c, auto num_acc_c, auto
346 num_pipeline_stage_c) {
347     constexpr unsigned num_thread_v = num_thread_c.value;
348     constexpr unsigned num_row_per_warp_v = num_row_per_warp_c.value;
349     constexpr unsigned num_acc_v = num_acc_c.value;
350     constexpr unsigned pipeline_stage_v = num_pipeline_stage_c.value;
351
352     // Runtime check against compile time constant wrapper
353     if (num_row_per_warp_v != static_cast<unsigned>(rows_per_warp)) return;
354
355     constexpr unsigned NUM_ROW_PER_BLOCK = (num_thread_v / WARP_SIZE) * num_row_per_warp_v;
356     TORCH_CHECK(M % NUM_ROW_PER_BLOCK == 0, "Output size ", M, " must be div by block rows ",
357 NUM_ROW_PER_BLOCK);
358
359     dim3 grid_dim(M / NUM_ROW_PER_BLOCK, seqlen);
360
361     rabbit_2bit_half_dyn_kernel<num_thread_v, num_row_per_warp_v, num_acc_v, pipeline_stage_v>
362         <<<grid_dim, num_thread_v, 0, stream>>>(
363             reinterpret_cast<const half*>(x.data_ptr<at::Half>()),
364             reinterpret_cast<const half*>(scale_g_0.data_ptr<at::Half>()),
365             reinterpret_cast<const uint32_t*>(Wbits.data_ptr<int32_t>()),
366             reinterpret_cast<const half*>(scale_h_0.data_ptr<at::Half>()),
367             reinterpret_cast<const half*>(scale_g_1.data_ptr<at::Half>()),
368             reinterpret_cast<const half*>(scale_h_1.data_ptr<at::Half>()),
369             reinterpret_cast<half*>(y.data_ptr<at::Half>()),
370             N, M);
371     C10_CUDA_KERNEL_LAUNCH_CHECK();
372 };
373
374 // Execute Sweep
375 sweep_num_thread("num_thread", num_thread, [&] (auto num_thread_c) {
376     sweep_row_per_warp("num_row_per_warp", num_row_per_warp, [&] (auto num_row_per_warp_c) {
377         sweep_num_acc("num_acc", num_acc, [&] (auto num_acc_c) {
378             sweep_pipeline_stage("num_pipeline_stage", num_pipeline_stage, [&] (auto num_pipeline_stage_c) {
379                 kernel_func(num_thread_c, num_row_per_warp_c, num_acc_c, num_pipeline_stage_c);
380             });
381         });
382     });
383     if (x.dim() == 1) {
384         y.squeeze_(0);
385     }
386     return y;
387 }

```